Vented methane-air explosion overpressure calculation - a simplified approach based on CFD

Jingde Li[1, a], Francisco Hernandez[2, b], Hong Hao[1, c], Qin Fang[3, d], Hengbo Xiang[3, e], Zhan Li[3, f], Xihong Zhang[1, g], Li Chen[3, h]

[1] Centre for Infrastructural Monitoring and Protection,
School of Civil and Mechanical Engineering, Curtin University,
Kent St, Bentley WA 6102, Australia

[2] Department of Civil Engineering, University of Chile,
Blanco Encalada 2002, Santiago, Chile

[3] State Key Laboratory of Disaster Prevention & Mitigation of Explosion &Impact,
PLA University of Science and Technology, Nanjing, Jiangsu 210007, China

[a]jingde.li@curtin.edu.au, [b]fraherna@gmail.com, [c]hong.hao@curtin.edu.au,
[d]fangqinjs@139.com, [e]xhb3188@163.com, [f]lz.9008@163.com,
[g]xihong.zhang@curtin.edu.au, [h]chenli1360@qq.com

Abstract

This paper presents new correlations developed through numerical simulations to estimate peak overpressures for vented methane-air explosions in cylindrical enclosures. A series of experimental tests are carried out first and the results are used to validate the numerical models developed with the commercial CFD software FLACS. More than 350 simulations consisting of 16 enclosure scales, 12 vent area to enclosure roof area ratios, 8 gas equivalence ratios and 9 vent activation pressures are then carried out to develop the Vented Methane-air Explosion Overpressure Calculation (VMEOC) correlations. Parameters associated with burning velocity and turbulence generation, oscillatory combustion and flame instabilities in vented gas

explosion are taken into account in the development of new correlations. Comparing to CFD simulations, the VMEOC correlations provide a faster way to estimate the peak overpressure of a vented explosion. Additionally, it is proved in this study that the VMEOC correlations are easier to use and more accurate than the equations given in the up-to-date industrial standard- NFPA-68 2013 edition.

Keywords: vented gas explosion, methane-air explosion, vent area, vent activation, peak overpressure.

1. Introduction

Gas explosions occurring in enclosed spaces can be found in many industrial and technological applications such as the tanks storing large amount of flammable Liquefied Natural Gas (LNG), tanker trucks for Liquefied Petroleum Gas (LPG) (Bariha et al., 2016) and commercial combustion engines, etc. (Ugarte et al., 2016). When a flammable gas-air mixture is ignited within a confined enclosure, there is an associated overpressure escalation in the combustion process. The overpressure escalation is caused by the hot burnt flame/gas expansion inside the confined space. It is this fast discharge of energy with its associated overpressure rise and high temperature flame growth that define a gas explosion (Tomlin et al., 2015).

The internal overpressure rise from a gas explosion can be large enough to create disastrous consequences (Sanchez, 2014). Numerous international events of oil and gas storage container explosions in the past decades (Chang and Lin, 2006) stimulate the development of explosion protection technology. These explosion protection/mitigation methods include air separation modules to inert flammable gas (Mitu et al., 2016) and combustible powder (Janes et al., 2014), explosion venting systems to ventilate flame growth in combustion (Ferrara et al., 2008; Janovsky et al., 2006; Wang et al., 2006), and water spray/mist deluge systems (Liang and Zeng, 2010) to handle large quantities of flammable vapor cloud (Shirvill, 2004), etc.

Amongst others, the cheapest and most practical explosion mitigation for the enclosure and its surroundings is the installation of a properly designed vent. In general, most oil and gas storage tanks are initially in fully-closed condition for internal and external services. However, when the gas explosion is accidently triggered by some natural factors or human errors, such as the Wynnewood explosion by lightning struck (Kurys, 2007), the appropriately designed tank should provide an adequate vent area, such as a frangible roof, to mitigate the flame and overpressure built-up. Furthermore, the vent panel or roof should be designed as light as reasonably practicable so that the vent activation pressure is low. The low vent activation pressure allows hot flame releasing in the early stage of explosion. Therefore, the rapid venting can result in a reasonably low and predictable overpressure.

So far, the vented gas explosion has been studied extensively for decades to provide understanding of the explosion phenomenon and mechanism (Bradley and Mitcheson, 1978; Cooper et al., 1986; Fairweather and Vasey, 1982; Mercx et al., 1992; Tamanini and Chaffee, 1992). Some mathematical and phenomenological models (Canu et al., 1990; Molkov et al., 1999; Rota et al., 1991; Runes, 1972) have been established and adopted in vented gas explosion design standards(EN-14994, 2007; NFPA-68, 2013), while some new models have been developed to consider more parameters, such as the effect of vent cover inertia in vented gas explosion (Molkov et al., 2004). In these standards, the vent opening size, peak overpressure for specific enclosure dimension, vent activation pressure and initial overpressure, etc. (Chao et al., 2011; Fakandu et al., 2015; Guo et al., 2016; Hochst and Leuckel, 1998; Siwek, 1996) are all taken into account in the vented explosion calculation. For example, NFPA-68 Standard on Explosion Protection by Deflagration Venting (NFPA-68, 1978) presented a model to estimate required vent area size for gas explosions on the basis of Runes' method (Runes, 1972). In 1988 and 1998, in order to improve the calculation accuracy of deflagration venting of gases, NFPA-68 standards adopted two different mathematical models (Bartknecht, 1993; Swift and Epstein, 1987) in different editions (NFPA-68, 1988, 1998). These old standards provide accurate results for certain scenarios, such as low-strength and small-scale enclosure cases, based on test work that bear no relationship to real in-process conditions (Swift, 1989). Afterwards, the updated version (NFPA-68, 2007) adopted equations for both low-strength and high-strength enclosures. The influence of internal obstacles and development of turbulent burning velocity in high-strength enclosures however were not accounted for. Therefore, in 2013, the latest NFPA-68 version (NFPA-68, 2013) included two important parameters to consider the flame wrinkling/stretching and instabilities in both of the small-scale and large-scale vented gas explosions. More accurate overpressure and vent area calculation results were achieved by using the NFPA-68 2013 edition's new correlations (Rodgers and Zalosh, 2013).

However, the 2013 edition of NFPA-68 was derived on the basis of the Swift-Epstein in 1980s (Epstein et al., 1986), the new equations have questionable technical suggestions since some features of the combustion process may not obey the statistical criteria used for their correlation generation. For example, for the maximum pressure developed in a vented enclosure during a vented deflagration below 0.5 bar-g, the vent release/activation pressure is not included in the correlations, but arbitrarily set below the maximum pressure of vented explosion. Therefore, the vent area calculation may be under/over predicted for sub-sonic flow cases with different vent release/activation pressures.

Moreover, the equations in the 2013 edition of NFPA-68 are relatively complex to use for sonic flow calculation. For instance, in order to consider the volume scaling turbulence adjustments of Rota's model (Rota et al., 1991), the iterative calculation has to be used. The vent diameter of enclosures then can be determined by taking the two parameters of the flame growth inside the enclosure and flame flow through the vent into account. For the calculation of the maximum pressure developed in a vented gas explosion, even more complicated backward induction algorithm needs to be adopted. Overall, the correlations of the NFPA-68 2013 edition are not straightforward for engineers to use.

Computational fluid dynamics (CFD) is by far the most detailed approach for quantifying the vented gas explosions. However, comparing to other empirical based correlations, CFD remains computationally expensive and labor intensive. There is, therefore, a need for the development of analytical models that can be applied with far less effort yet still capture the principal mechanisms for flame propagation and flame wrinkling in vented explosions. In this paper, a phenomenological study is conducted to develop simplified correlations based on CFD. The widely-recognized CFD commercial software FLACS, which itself has been validated over the last decades against a large number of experiments and previous work (Bleyer et al., 2012; Hansen et al., 2010; Ma et al., 2014; Middha et al., 2010; Middha et al., 2009; Pedersen et al., 2012; Pedersen and Middha, 2012) have been utilized.

A series of field blast tests was conducted by the authors. Along with previously performed large-scale experiments by other researchers available in literature, the test data is used to validate FLACS simulations results that would be applied towards the development of the Vented Methane-air Explosion Overpressure Calculation (VMEOC) correlations. Over 350 CFD simulations are conducted to account for parameters of gas concentration, burning velocity, vent activation pressure, and turbulence generation in different vent area sizes and enclosure geometries. Furthermore, CFD simulation results are compared with the maximum overpressures calculated by using the VMEOC and the 2013 edition of NFPA-68 standards. It is proved that the VMEOC correlations provide more accurate overpressure calculation results than that of the vented gas explosion standard NFPA -68 2013 edition, and greater implementation speed comparing with CFD simulations.

2. Experimental gas explosion testing

In the experimental investigation of this study, the cylindrical tanks are designed according to American Petroleum Institute Standard (API-650, 2007). The dimension of all tanks is 1.5m in diameter and 1.0m in height (i.e. volume of 1.77m^3) with a conical roof slope of 1/16.

2.1 Experimental details

Three types of tanks with different vents are designed, as shown in Fig. 1. Type 1 tank has the equally spaced stitch welds at the connection of roof to the shell. Type 2 tank has stitch welds and a hinge opening on the roof. And two vent panels with low activation/opening pressure are mounted on the roof of Type 3 tank.

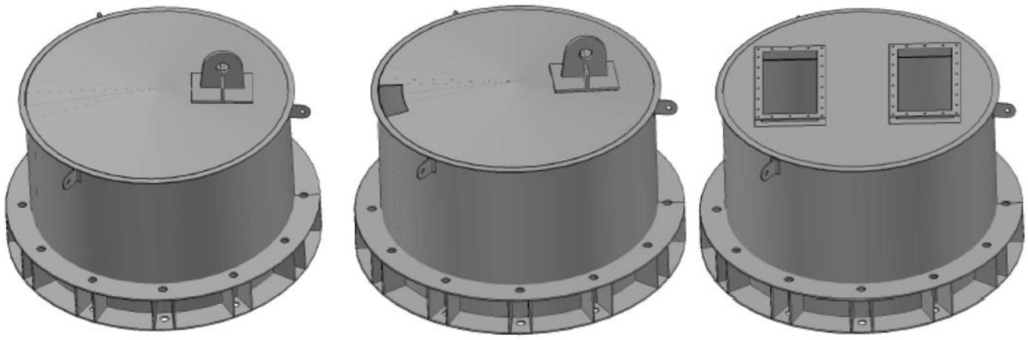

(a) Type 1 tank **(b) Type 2 tank** **(c) Type 3 tank**

Fig. 1 Tanks with different vents

The circular bottom plate of each tank is anchored to a circular reinforced concrete foundation, so that tanks are stationary when gas explosion occurs inside. High strength bolts of 25.4mm diameter are used. Two PSB pressure sensors on the tank wall are mounted by using hex nuts, and rubber washers are used to ensure the impermeability of equipment. High Speed Video Camera (HSVC) tracker panels are attached on tank roof and shell, as seen in Fig. 2. Pressure transducers with 1000 kPa pressure monitoring capacity are bolted on inner wall of the tank. Signals from pressure transducers are logged on a 16-Bit A/D converter sampling at 50 kHz.

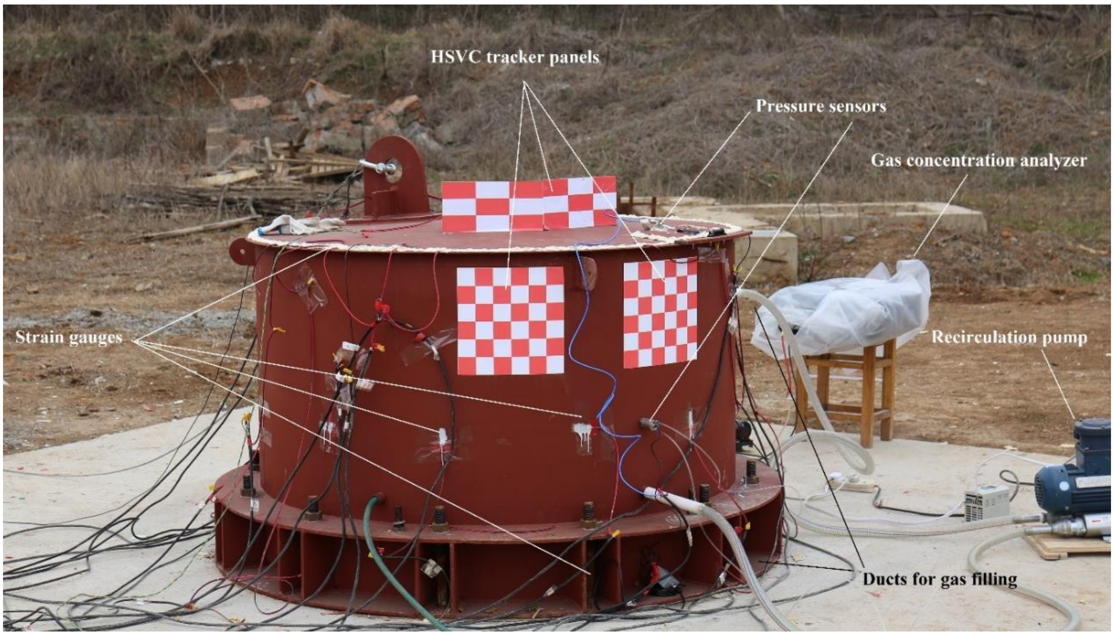

Fig. 2 Installation of measurement system

Four isolation flange valves of 0.75 inch (about 1.9 cm) diameter are mounted on the shell for air discharge, gas inlet and outlet. 24 and 22 equally spaced stitch welds (3mm leg) are used for Type 1 and Type 2 tanks, respectively. Type 3 tank has continuously welds (5 mm leg) instead. A polyethylene file is installed under the vent panels to ensure gas is not leaking during gas filling process. Low strength latex foam sealant, as seen in Fig. 3, is used to seal the top roof holes and welding gaps.

Fig. 3 Latex foam sealant used to seal weld gaps

High Speed Video Camera (HSVC) is placed at 10m from the tank. The resolution and shutter time of the HSVC are 2000-3000 fps and 1/50000, respectively. Through-The-Lens (TTL) system is used to synchronize HSVCs with sensors. The inlet flammable methane-air mixture is controlled by Gas Flow Control System (GFCS), as illustrated in Fig. 4. A vent duct is used to release gas from the tank to maintain the initial atmospheric pressure. In addition, a recirculation pump and an infrared methane analyzer, as seen in Fig. 5, are used to measure and control gas-air concentration.

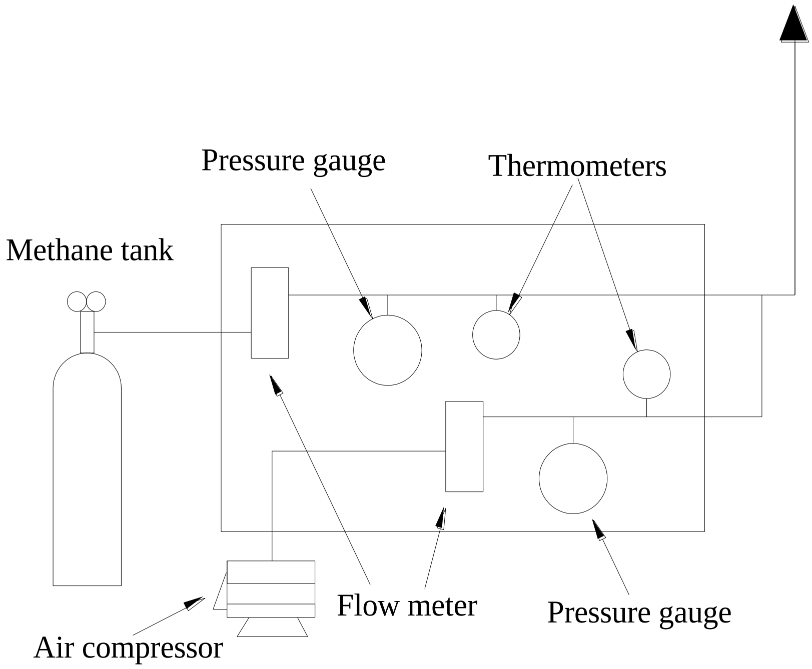

Fig. 4 Gas Flow Control System (GFCS) scheme

(a) Recirculating water and air pump **(b) Infrared gas concentration analyzer**

Fig. 5 Equipment in GFCS scheme

A set of ionization probes and an electric spark plug, as seen in Fig. 6, are used as ignition source, which is located at the center of tank. The steel Q345B with tensile strength in the range of 470 MPa to 630 MPa, and yield strength of 345 MPa is used as the tank material. The installation of hinged venting panel and two explosion venting EGV panels (REMBE, 2015) are seen in Fig. 7, the welding with yield strength of 450 MPa and tensile strength of 530 MPa are used for all the three different tank types. Five field gas explosion tests are conducted; the experimental conditions are reported in Table 1.

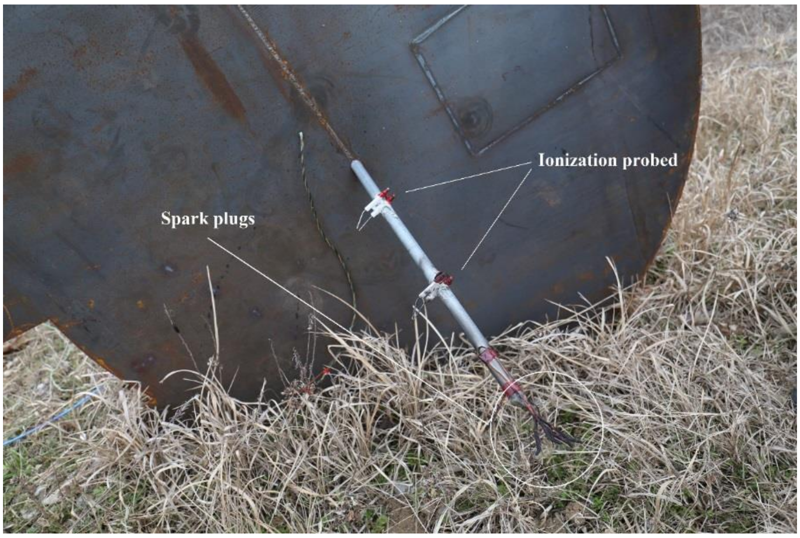

Fig. 6 Ionization probes and electric matches

(a) Stitch-Welds for Tank 1 **(b) Hinge cover for Tank 2** **(c) REMBE vent panel for Tank 3**

Fig. 7 Explosion venting installation

Table 1 Condition of field gas explosion tests

Case No.	Tank type	Vent opening condition	Fuel-air concentration
1.	Type.1 –No.1	24 stitch welds with roof opening	6.5 vol% methane
2.	Type.2 –No.1	22 stitch welds with a hinged vent panel	6.5 vol% methane
3.	Type.2 –No.2	22 stitch welds with a hinged vent panel	6.5 vol% methane
4.	Type.2 –No.3	22 stitch welds with a hinged vent panel	9.5 vol% methane
5.	Type.3 –No.1	2 explosion vent panels mounted on the roof	6.5 vol% methane

2.2 Experimental results and discussion

Fig. 8 shows some of HSVC snapshots of these 5 different vented gas explosion scenarios. As seen in Fig. 8 (a), the overpressure of gas explosion is big enough so that the 24 equally spaced welds are fully yielded in Type 1 tank blast test, the roof is propelled over 10 meters away from the tank in the end of explosion. Three different explosion cases are carried out for Type 2 Tank, where the explosion case No. 2 and No. 3 have 6.5 vol% methane-air concentration (Fig. 8 (b) and (c)), the hinged panels provide earlier ventilation of gas explosion, due to the fact that the hinged panels can be activated to open under small explosion pressure. Therefore, the internal overpressures are reduced significantly so that the reduced maximum pressure is lower than the welding failure strength. However, when the methane-air concentration is increased from 6.5 vol% to 9.5% in case No. 4 (Fig. 8 (d)), a roof failure is seen after the hinge panel opens. This is because the stoichiometric concentration explosion generates higher overpressure than the internal overpressure in 6.5 vol% methane explosion, which eventually lifts up the tank roof after welding failure. As for the explosion case No. 5, the two symmetrical explosion vent panels are activated simultaneously. The REMBE vent panel provides large venting area and early ventilation, which rapidly mitigates the internal overpressure of explosion.

(a) Case No. 1 venting **(b) Case No. 2 venting**

(c) Case No. 3 venting **(d) Case No. 4 venting** **(e) Case No. 5 venting**

Fig. 8 High Speed Video Camera snapshots for 5 explosion cases

Internal overpressures are monitored at height 500mm on tank wall. Fig. 9 shows the recorded overpressure-time histories in 5 different field tests. Experimental data is not filtered, and the ignition times for all cases are at t=0.0 s. Together with the records in HSVC, different lines can be plotted to indicate the vent activation time, maximum internal overpressure time and zero internal overpressure time, etc.

Firstly, the initiation of the roof failure time is recorded at 554ms for case No. 1 explosion, the time that internal overpressure drops to zero is 572.9ms, and the roof completely detaches the tank at time of 639.5s (Fig. 9 (a)). For case No. 2, the activation of the hinged vent panel is initiated at 294ms, the maximum overpressure is recorded at 514.8ms, and the reduced internal pressure drops to zero at 1550ms (Fig. 9 (b)). Fig. 9 (c) shows the venting activation time at 344ms for case No. 3, the peak overpressure is recorded at 735ms. In addition, HSVC indicates the venting activation time for case No. 4 (Fig. 9 (d)) is at 181ms, the stitch welds on the right side and left side start to fail at time of 405.6ms and 426.3ms respectively, the maximum internal overpressure is observed at 435ms. Last but not least, Fig. 9 (e) shows the overlapping of vent panel activation time and the maximum overpressure of case No. 5 occurs at 372ms, the internal overpressure drops to zero at t=389.2ms.

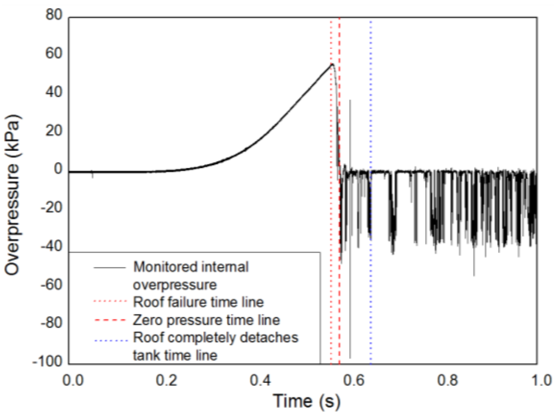

(a) **Pressure-time history for Case No. 1**

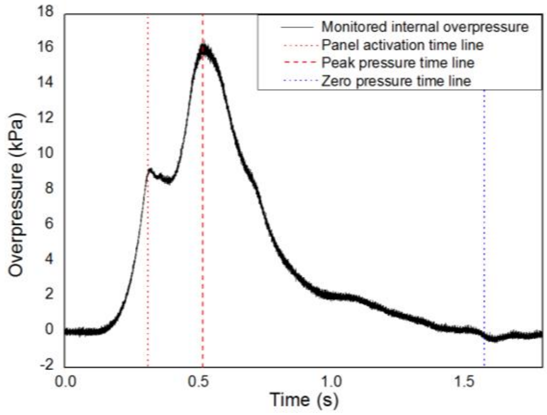

(b) **Pressure-time history for Case No. 2**

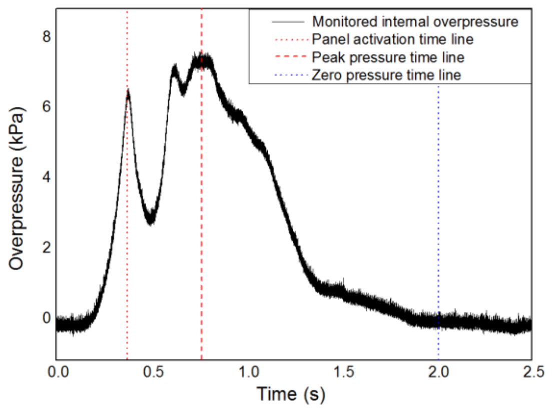

(c) **Pressure-time history for Case No. 3**

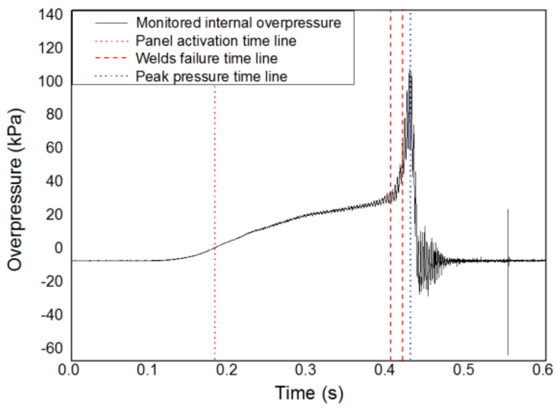

(d) **Pressure-time history for Case No. 4**

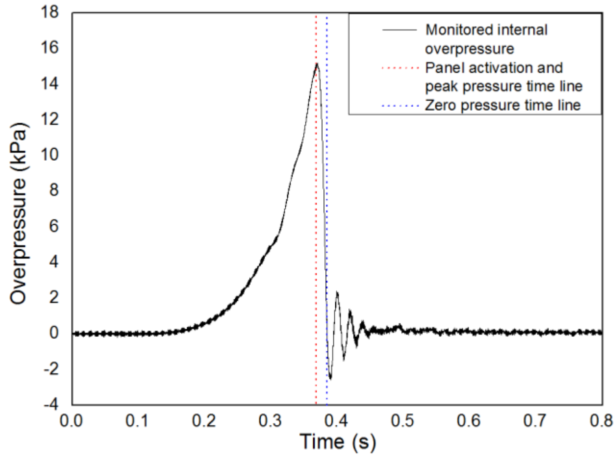

(e) **Pressure-time history for Case No. 5**

Fig. 9 Monitored internal overpressures for 5 explosion cases

Table 2 Summary of experimental results

Case No.	Tank type	Methane-air concentration	Vent activation pressure P_{act} (kPa)	Roof failure pressure P_{rof} (kPa)	Max internal pressure P_{max} (kPa)
1.	Type.1 –No.1	6.5 vol%	-	61.1	61.1
2.	Type.2 –No.1	6.5 vol%	9.0	-	16.5
3.	Type.2 –No.2	6.5 vol%	6.6	-	7.5
4.	Type.2 –No.3	9.5 vol%	6.3	47.0	115.0
5.	Type.3 –No.1	6.5 vol%	15.0	-	15.0

Table 2 summarizes the experimental data of the monitored vent activation pressure P_{act}, roof failure pressure P_{rof}, and the maximum reduced pressure P_{max}. Specifically, without a vent panel, the roof of case No. 1 tank is damaged and lifted up under an internal overpressure of 61.1kPa, whereas Type 2 tanks in case No. 2, No. 3 and No. 4 with side vent panels experience activations of the vent panels first. When a low gas-air concentration of 6.5 vol% is employed for Test 1 and 2 of Type 2 tanks, the opening of vent panel (2% of the cross section area of the tank) is sufficient to mitigate the internal overpressure at early stage to avoid the roof failure. Comparing to Test 1 of Type 2 tank (P_{act}=9 kPa and P_{max}=16.5kPa), the lower vent activation pressure P_{act} (6.6 kPa) in Test 2 of Type 2 tank resulted in lower peak reduced internal overpressure P_{max} (7.5 kPa). However, when the gas concentration increases to stoichiometric concentration (9.5 vol%) in Test 3 of Type 2 tank, a faster and stronger gas deflagration is observed. The opening of vent panel is followed by roof failure, which is due to the fact that the combustion of stoichiometric concentration scenario is faster than that of other low gas concentration cases, and the continuingly increasing overpressure (115 kPa) exceeds the stitch welding capacity, which eventually tears off the tank roof. On Type 3 tank, two large vent panels with 20.9% of the roof area are installed. Unlike Type 2 tank explosion, there is no up-and-down between P_{act} and P_{max}, the vent area is large enough so that the flame growth is inhibited when the two panels open simultaneously, the ventilation greatly mitigates internal overpressure and limits P_{max} to be equal to P_{act}.

All pressure sensors and HSVC work properly and synchronized. It is seen in Fig. 8 that roof failure is due to the failure of the stitch welds, local strain hardening only occurs near the welding on roof. However, plastic collapse of the compression ring, buckling of the tank shell and roof are not observed, which is because of the high axial stiffness of the compression ring. Therefore, in the following numerical modelling, these tanks are ideally assumed as rigid in CFD simulation.

3. CFD simulation and validation

The small-scale experiments investigated above are then used along with other previously conducted large-scale tests (Hochst and Leuckel, 1998; Moen et al., 1982) to calibrate CFD model.

The commercial software FLACS (version 10.4), which is a specialized CFD solver for the prediction of blast loads, is utilized in this study. FLACS uses $k{-}\varepsilon$ model for turbulence simulation, and a "distributed porosity concept" is employed in FLACS to represent complex three-dimensional geometries by using a Cartesian grid. On-grid and sub-grid objects with computed porosity value are used to represent obstacles and walls in FLACS, Navier-Stokes equations are solved on the 3D Cartesian grid. The conservation equations for mass, momentum, enthalpy, turbulence and species, closed by the ideal gas law are included (Pedersen and Middha, 2012). The Simple Interface Flame (SIF) model, that the flame is resolved and modelled as an interface to ensure good representation of flame area in a coarse grid, is applied in this study to handle compressible flows.

3.1 Numerical models of FLACS

The mathematical models of FLACS (Gexcon, 2015) are given in (Arntzen, 1998; Ferrara et al., 2006; Hjertager, 1984, 1993).

For a general variable, the differential equation, which is based on Reynolds averaged mass, momentum and energy balance equations, is expressed as follows using standard symbols:

$$\frac{\partial}{\partial t}(\rho\varphi)+\frac{\partial}{\partial x_j}(\rho u_j\varphi)-\frac{\partial}{\partial x_j}\left(\Gamma_\varphi\frac{\partial\varphi}{\partial x_j}\right)=S_\varphi\,;\Gamma_\varphi=\frac{\mu_{eff}}{\sigma_\varphi} \tag{1}$$

where f denotes a general variable, ρ is the gas mixture density, x_j is the coordinate in *j*-direction, u_j is the velocity component in *j*-direction, Γ_φ is the effective (turbulent) diffusion coefficient, μ_{eff} is the effective turbulence viscosity and S_φ is a source term.

A summary of all the governing equations needed for a typical reactive gas dynamic calculation are presented below.

The state equation of an ideal gas:

$$pW=\rho RT \tag{2}$$

where p is the pressure, R is the universal gas coefficient T is temperature and W is the molar weight of the gas mixture.

The continuity equation:

$$\frac{\partial\rho}{\partial t}+\frac{\partial}{\partial x_j}(\rho u_j)=0 \tag{3}$$

The momentum balance equation:

$$\frac{\partial}{\partial t}(\rho u_i)+\frac{\partial}{\partial x_j}(\rho u_j u_i)=-\frac{\partial p}{\partial x_i}+\frac{\partial}{\partial x_j}(\sigma_{ij}) \tag{4}$$

The energy balance equation:

$$\frac{\partial}{\partial t}(\rho h)+\frac{\partial}{\partial x_j}\left(\rho u_j h\right)=\frac{\partial}{\partial x_j}\left(\Gamma_h \frac{\partial h}{\partial x_j}\right)+\frac{\partial p}{\partial t}+u_j \frac{\partial p}{\partial x_j} \tag{5}$$

where σ_{ij} is the flux of momentum and h is the enthalpy.

The solver accounts for dissipation of turbulent kinetic energy with a modified k-ε model (Arntzen, 1998; Hjertager, 1993).

The equation for turbulent kinetic energy:

$$\frac{\partial}{\partial t}(\rho k)+\frac{\partial}{\partial x_j}\left(\rho u_j k\right)=\frac{\partial}{\partial x_j}\left(\frac{\mu_{eff}}{\sigma_k}\frac{\partial k}{\partial x_j}\right)+G-\rho\varepsilon\,;\ \ G=\sigma_{ij}\frac{\partial u_j}{\partial x_i} \tag{6}$$

The equation for dissipation of turbulent kinetic energy:

$$\frac{\partial}{\partial t}(\rho\varepsilon)+\frac{\partial}{\partial x_j}\left(\rho u_j \varepsilon\right)=\frac{\partial}{\partial x_j}\left(\frac{\mu_{eff}}{\sigma_\varepsilon}\frac{\partial \varepsilon}{\partial x_j}\right)+1.44\frac{\varepsilon}{k}G-1.79\rho\frac{\varepsilon^2}{k} \tag{7}$$

where G is the generation rate of turbulence.

The combustion process is treated as a single step irreversible reaction with finite reaction rate between fuel and oxidant. The reaction scheme results in mixture composition being determined by solving for only two variables, namely mass fraction of fuel m_{fu}, and the mixture fraction f (Hjertager, 1984):

$$\frac{\partial}{\partial t}\left(\rho m_{fu}\right)+\frac{\partial}{\partial x_j}\left(\rho u_j m_{fu}\right)=\frac{\partial}{\partial x_j}\left(J_{fu,j}\frac{\partial \varepsilon}{\partial x_j}\right)+R_{fu} \tag{8}$$

$$\frac{\partial}{\partial t}(\rho f)+\frac{\partial}{\partial x_j}\left(\rho u_j f\right)=-\frac{\partial}{\partial x_j}\left(J_{f,j}\right) \tag{9}$$

where R_{fu} is the time mean rate of combustion of fuel, $J_{fu,j}$ and $J_{f,j}$ are the diffusive fluxed in the x_j-direction.

A pressure correction equation, which is based on conservation of mass, is then used to obtain the developed pressure. The pressure correction algorithm in this study is based on the modified correction routine - Simple Interface Flame model (SIF), which satisfied the equation of state and gives the correct in-flow and out-flow density in addition to pressure.

The correct density in reactant and velocity are the sums of guessed and corrected values (i.e. reactant and velocity), and can be described as functions of the pressure correction:

$$P_c = P^{\#} + P^{''} \tag{10}$$

$$\rho_R = \rho_R^{\#} + \rho_R^{''} = \rho_R^{\#}(1 + \frac{P^{''}}{\kappa P^{\#}}) \tag{11}$$

$$u = u^{\#} + u^{''} = u^{\#} + d_w(P^{''}) \tag{12}$$

where P_c is the corrected pressure, $P^{\#}$ is the guessed pressure, $P^{''}$ is the pressure correction, ρ_R is the corrected density , u is the corrected velocity, κ is a constant and d_w is the coefficient of the pressure-difference term.

FLACS solves the equations above such that the pressures from previous time step, the momentum equation gives a velocity field, which will be corrected along with the updated pressure and density field (Patankar, 1980).

3.2 Numerical modelling of small-scale tanks and comparison with experiments

Fig. 10 shows the 3D geometries of the tested 3 tank types in FLACS. The ambient temperature of 10 degree and atmosphere pressure 101 kPa are used as initial condition. Tank roof and wall are assumed to be rigid during explosion. In the combustion region, all grid cells are cubical in order to reduce the deviations of flame propagation and overpressure built-up. A minimum of 15 grid cells are guaranteed at vent opening. From vent panel to boundaries, grid cells are stretched, the aspect ratio of the grid increment is controlled within 10%. Sensitivity study is conducted, the grid cell size within the combustion region inside tank is chosen as 0.05m, and Eulerian boundary condition is used for all simulations. The inviscid flow equations (Euler equations) are discretised for the boundary elements, which means that the momentum and continuity equations are solved on the boundary in the case of outflow. The ambient pressure is used as the pressure outside the boundary.

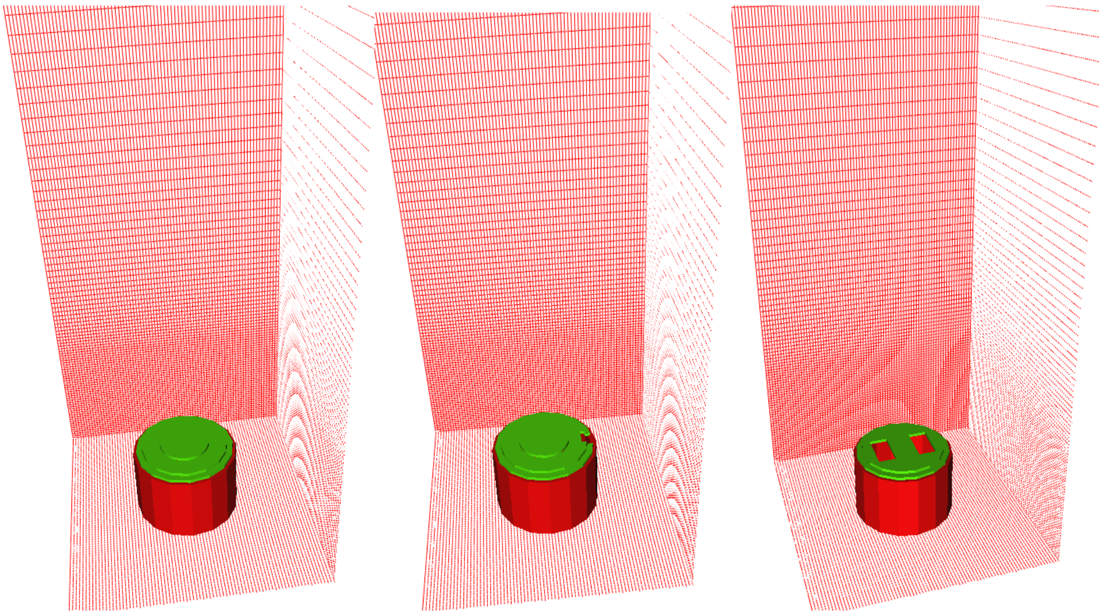

(a) Type 1 tank **(b) Type 2 tank** **(c) Type 3 tank**

Fig. 10 FLACS simulation models for different tank types

Monitor points are located close to tank’s vent panel at height of 1m and on tank’s wall at height of 0.5m and 0.75m as seen in Fig. 11 (a). The ignition point (Fig. 11

(b)) is at the center of the tank corresponding to the experiment setup described in Section 2.

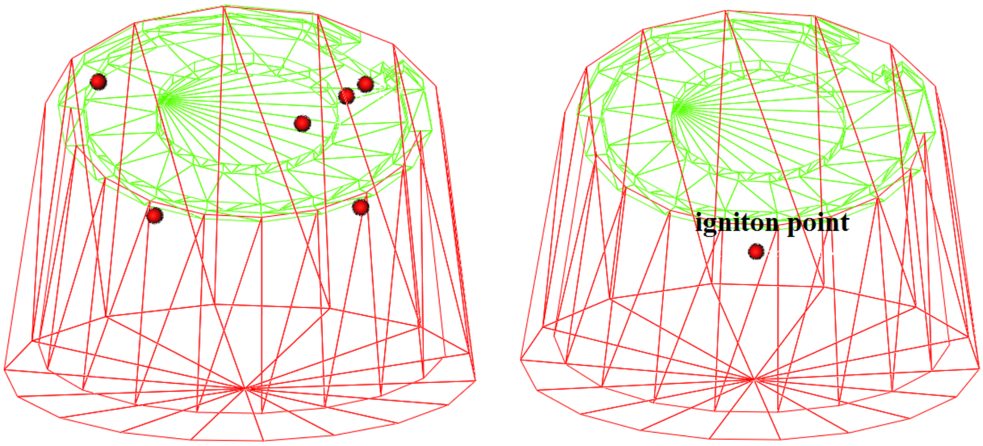

(a) Locations of monitor points **(b) Ignition point location**

Fig. 11 Locations of monitor points and ignition

Pressure relieve panels in FLACS are used to model the vent panels in Type 2 and Type 3 tanks, the yellow color pressure relive panels are shown in Fig. 12. According to Table 2, the vent opening pressures of these vent panels for Type 2 tanks in No. 1, 2 and 3 tests are set as 0.09, 0.066 and 0.063 bar-g, respectively, and the vent opening pressure of Type 3 tank (Fig. 12(b)) is 0.15 bar-g in FLACS. Hinged panel with panel weight of 1 kN/m^2 is used to simulate the light-weight side vent and REMBE vent panels. Initial and final porosities of all panels are set as 0.0 and 1.0, respectively, which represent the initially closed vent status and fully opened vent condition of these tanks.

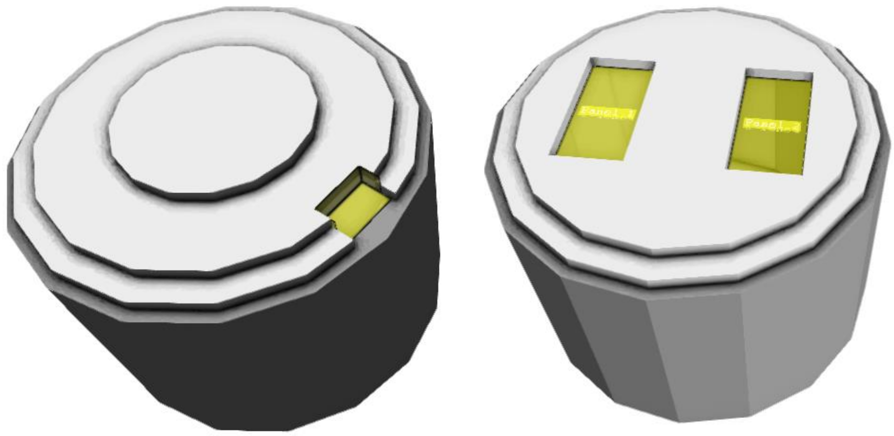

(a) Pressure relieve panel in Type 2 tank **(b) Pressure relieve panels in Type 3 tank**

Fig. 12 Pressure relieve panels in FLACS geometry

In FLACS, the overpressure-time history is extracted from monitor point on the tank wall at 0.5m height for each explosion case. The corresponding experimental data of overpressure-time histories in Fig. 9 are filtered and compared with numerical data calculated by FLACS, and shown in Fig. 13. It is seen that the peak overpressures and pressure built-up tendencies predicted by FLACS agree well with the experimental data in all explosion cases. Precisely, for large vent area scenarios, such as Type 1 tank (Fig. 13 (a)) with a frangible roof and Type 3 tank (Fig. 13 (e)) with two REMBE vent panels, reduction of internal pressure starts instantly along with the activation of roof failure or panel opening, which is seen in both the numerical and experimental results. However, for small vent panel cases, such as Type 2 tanks with a side vent panel of 2% roof area size, the small size ventilation is not sufficient to completely suppress flame expansion and pressure growth. Therefore, the first peak overpressure P_{act} is followed with another peak overpressure P_{max}, which is resulted from the external explosion outside the chamber that the maximum flame area is achieved.

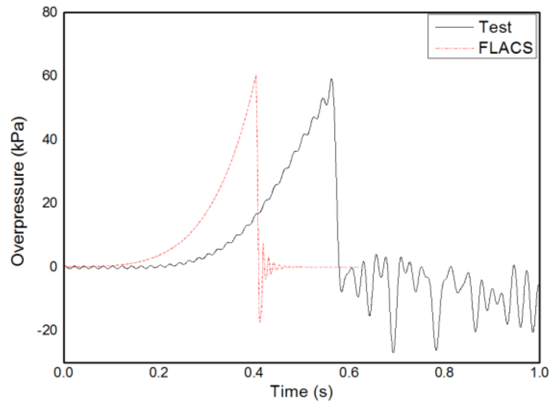

(a) Pressure-time history for Type 1- No.1 Case

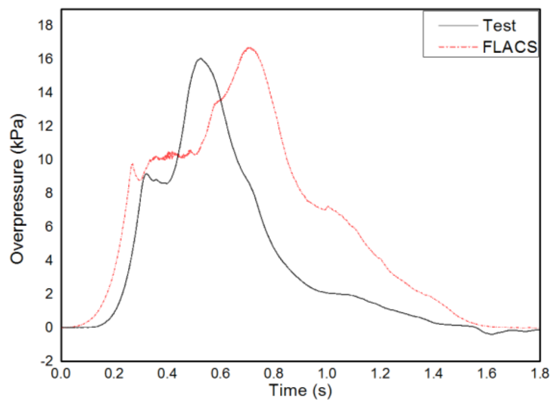

(b) Pressure-time history for Type 2- No.1 Case

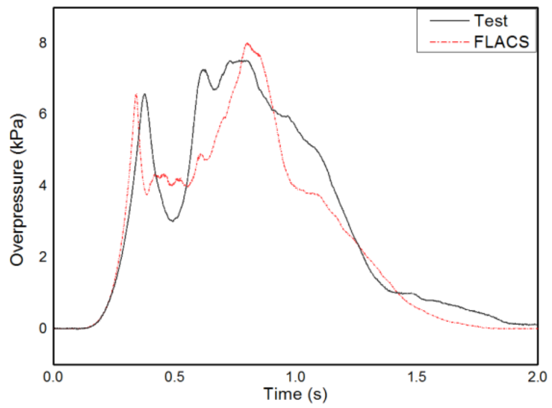

(c) Pressure-time history for Type 2- No.2 Case

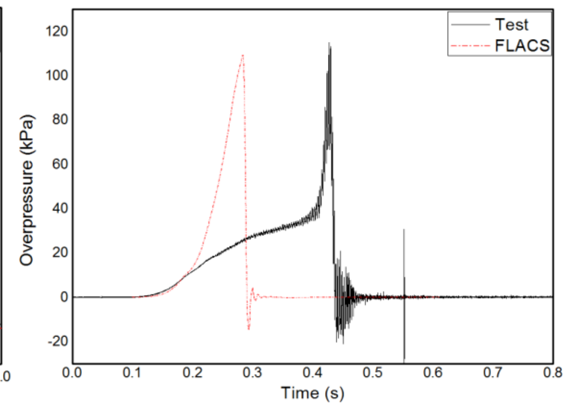

(d) Pressure-time history for Type 2- No.3 Case

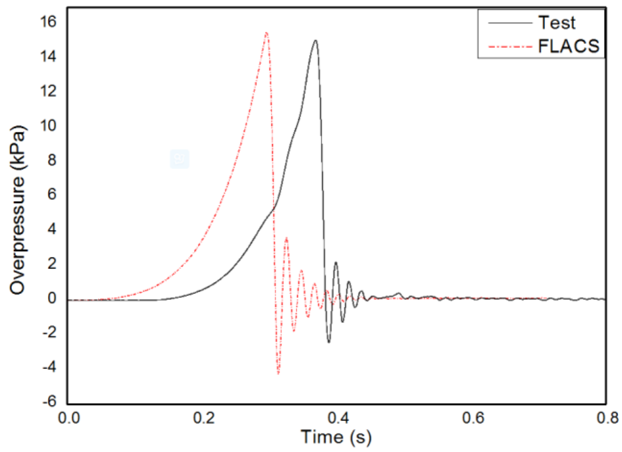

(e) Pressure-time history for Type 3- No.1 Case

Fig. 13 Comparison of FLACS simulation results and experimental data

3.3 Numerical modelling of large-scale silo and comparison with experiments

Having validated the numerical simulations of small-scale tanks with satisfactory results, large-scale vented methane explosion simulations are then carried out.

A $50m^3$ cylindrical silo with a diameter of 2.5m and a height of 10m subjected to methane/air mixture explosion (Hochst and Leuckel, 1998), as seen in Fig. 14, is numerically simulated by using FLACS. The grid cell size inside tank is set as 0.05m, Eulerian boundary condition is used. Hinged pressure relieve panel with vent activation pressure of 0.02 bar-g is used, the vent size is 50% of the roof area. The silo is filled with 10.2 vol% methane-air mixture. In terms of the initial condition in FLACS, the characteristic velocity u_o , relative turbulence intensity I_T and turbulence length scale l_{LT} are set as 0.29 m/s, 0.1 and 0.045m, respectively.

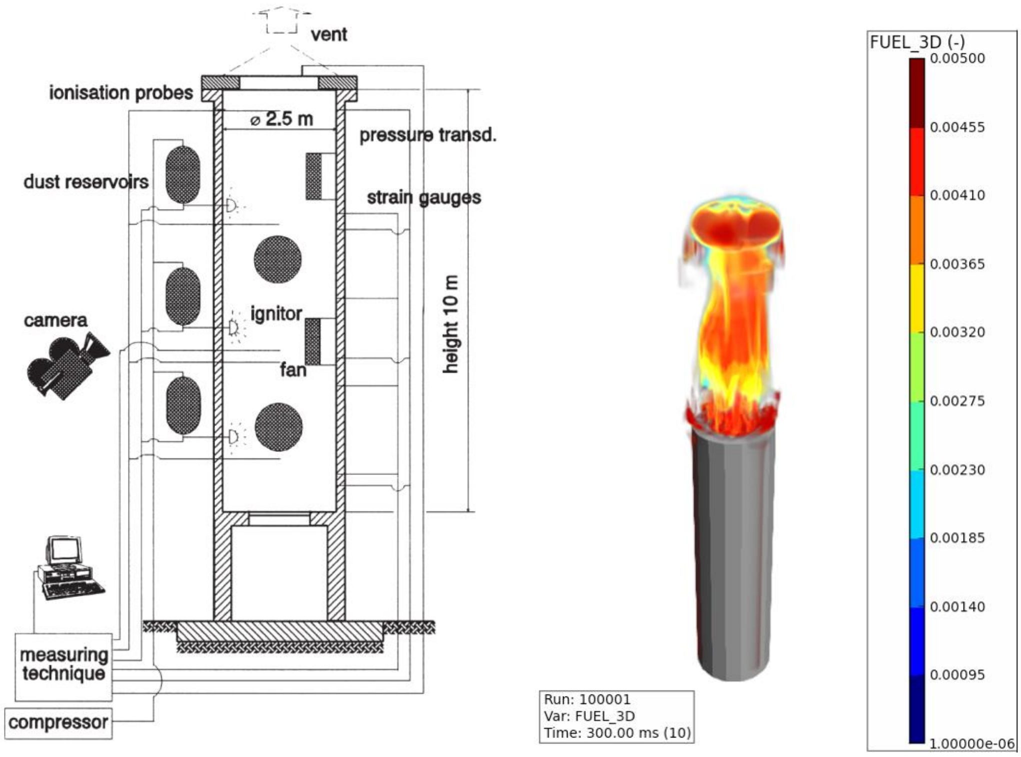

(a) Experimental setup (Hochst and Leuckel, 1998) **(b) 3D view in FLACS**

Fig. 14 Methane explosion test configuration and numerical modelling in FLACS

Fig. 15 shows the comparison of overpressure-time histories obtained from the test (Hochst and Leuckel, 1998) and FLACS simulation. It is observed that the maximum overpressure (second peak) in FLACS is slightly higher than the experimental data, while the first peak overpressure related to the vent activation pressure in FLACS is marginally lower than that in the test. Overall, the numerical simulation results of overpressure-time history agree with the large-scale silo test results well.

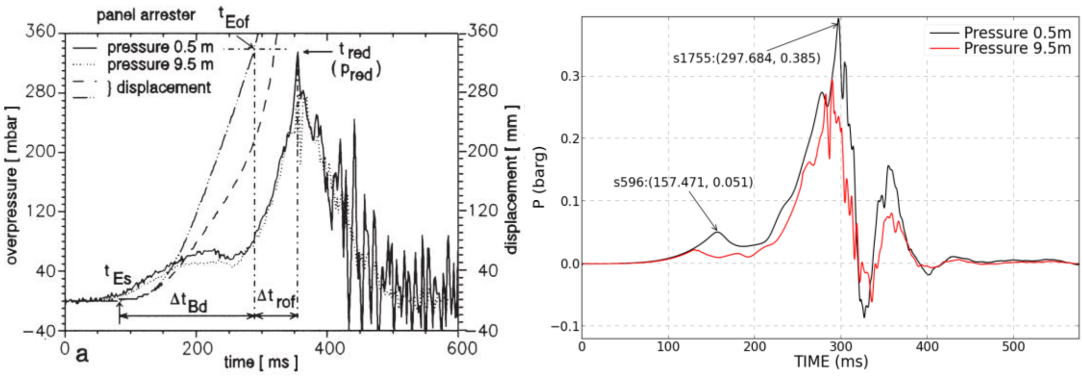

(a) Experimental data (Hochst and Leuckel, 1998) **(b) FLACS simulation results**

Fig. 15 Pressure-time history comparison between experimental data (Hochst and Leuckel, 1998) and FLACS results

3.4 Numerical modelling of large-scale tube with orifice plates and comparison with experiments

The above investigations of small-scale methane-air explosion tests by authors and large-scale tests by (Hochst and Leuckel, 1998) correspond to two different volumes (1.77 m^3 and 50m^3) only. In order to verify the accuracy of CFD simulations of other scale methane-air explosions, ideally more tests should be carried out and the test data used to validate the numerical simulation. Unfortunately such testing data are not easily available in open literature and not straightforward to obtain. In this study the experiments of methane-air explosions in large combustion vessels with orifice plates carried out by (Moen et al., 1982) are utilized to calibrate FLACS simulation results.

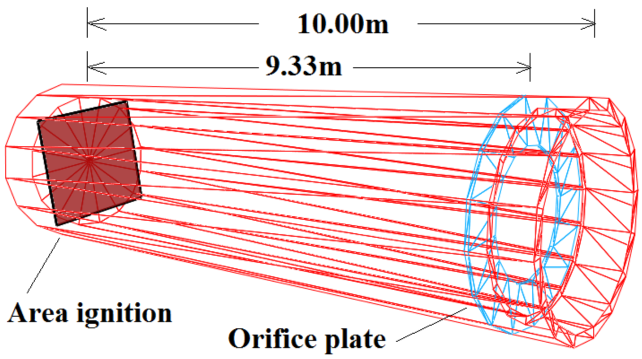

(a) Orifice plate installed at 9.33m from ignition

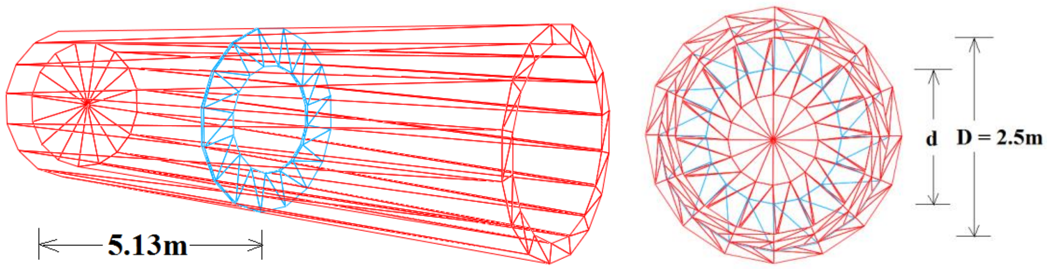

(b) Orifice plate at 5.13m from ignition **(c) Orifice plate detail**

Fig. 16 3D Large-scale Methane-air vented explosion configuration in FLACS

As seen in Fig. 16, the cylindrical combustion enclosure is a 10m long, 2.5m diameter steel tube with a volume of 49.09 m^3. The end of tube on the left hand side is closed and attached to ignition source, whereas the tube end on the another side is fully open. In FLACS, area ignition is utilized to simulate the planer ignition, which can expose the explosion flame covering the entire tube cross-section area, as shown in Fig. 16 (a). In order to categorize the vented methane explosion scale, the volume of the confined region is defined as the cross section area multiply the distance from ignition to orifice plate in far end. 10 different explosion cases with different confined volumes are summarized in Table 3, for each explosion case, orifice plate is placed at a different location (for example, Case No. 8 as seen in Fig. 16 (a) and Case No. 6 as seen in Fig. 16 (b)). The orifice plates are designed with different blockage ratios (Fig. 16 (c)), which is defined as $B.R. = 1-(d/D)^2$. Meanwhile, the blockage ratio of the orifice plate reflected the Vent Area Ratio (*VAR*) of the confined vessel as $VAR=1- B.R.$. Additionally, methane-air mixture of 9.5 vol% is used in all FLACS simulations. The grid cell size inside the combustion vessel is set as 0.05m, Eulerian boundary condition is used.

Table 3 Summary of experimental setup (Moen et al., 1982) & comparison of experimental data and numerical results

Case No.	Orifice plate No. & distance from ignition	*B.R.* of orifice plate	Volume of confined region (m^3)*	Peak pressure in tests (bar-g)	Peak pressure in FLACS (bar-g)
1	No plate	0.00	49.09	0.12	0.07
2	1 plate @ 1.65m	0.84	8.10	2	1.71
3	1 plate @ 1.65m	0.30	8.10	0.66	0.65
4	1 plate @ 1.65m	0.16	8.10	0.5	0.42
5	1 plate @ 5.13m	0.16	25.18	0.3	0.64
6	1 plate @ 5.13m	0.50	25.18	2.7	2.75
7	1 plate @ 5.13m	0.84	25.18	3.8	4
8	1 plate @ 9.33m	0.50	45.80	0.9	0.67
9	2 plates @ 5.13m & 9.33m	0.30	45.80	1.5	1.7
10	2 plates @ 1.65m & 5.13m	0.50	25.18	4.05	4.23

*Volume is equal to the cross section area multiply the distance from ignition to orifice plate in far end

The peak overpressures recorded in different monitoring points inside the combustion vessel are extracted in FLACS to compare with experimental data. It is seen from Fig. 17 that the agreement between FLACS simulation data and laboratorial results has an R-squared factor of 98.32%, which means the overall peak internal overpressures of vented gas explosion are well predicted by FLACS. However, it is noteworthy that there is a relatively greater difference between the FLACS simulation result and experimental data in case No. 5, as seen in Table 3. The main reason is that the blockage ratio of the orifice plate in case No. 5 is only 16%, which results in a small ring-shaped confinement. In FLACS, the thickness of the orifice plate has to be at least one grid cell size, therefore, the ratio of the plate's thickness to the ring-shaped area in case No. 5 becomes larger than that of the other cases. The 16% BR orifice plate with great ratio of thickness to cross-section area is treated as an obstacle with large surface area in FLACS. Unlike case No. 4 where the orifice plate is placed near the ignition, case No. 5 has the orifice plate in the middle of the enclosure. In such a position, the orifice plate acting as an obstacle enhances the turbulence development, which eventually results in overpressure over-prediction.

The summarized comparison of all experimental results (i.e. data from the authors, Moen et al. (1982) and Hochst and Leuckel (1998)) and FLACS simulations data is shown in Fig. 18. Overall, FLACS modelling data are shown yielding good predictions of internal pressure from vented explosion. The zoomed-in figure on right corner indicates even better agreement between the authors' data and test results.

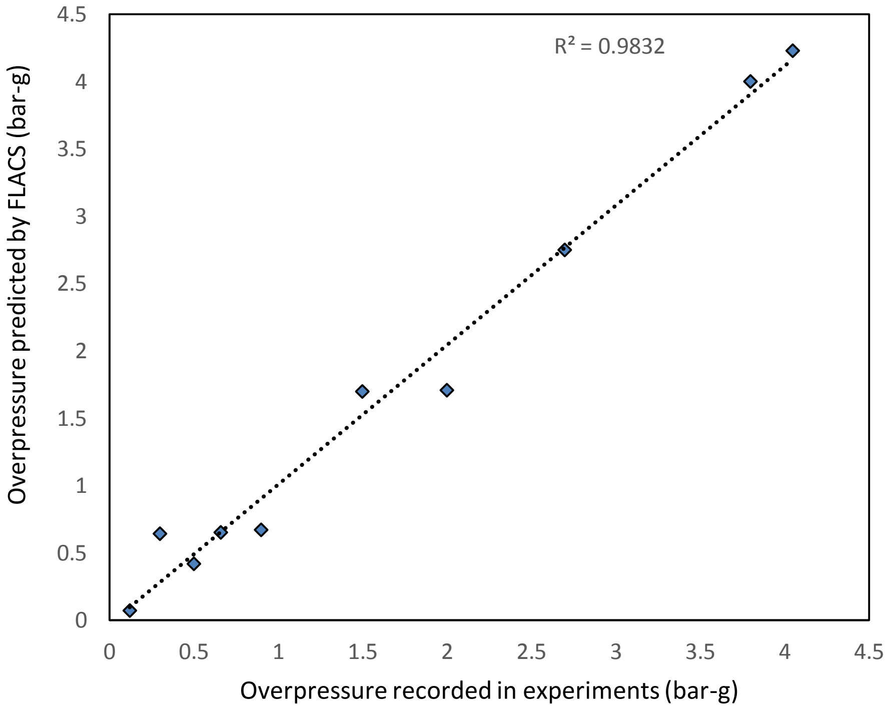

Fig. 17 Comparison of peak overpressures predicted by FLACS and peak overpressures monitored in experiments

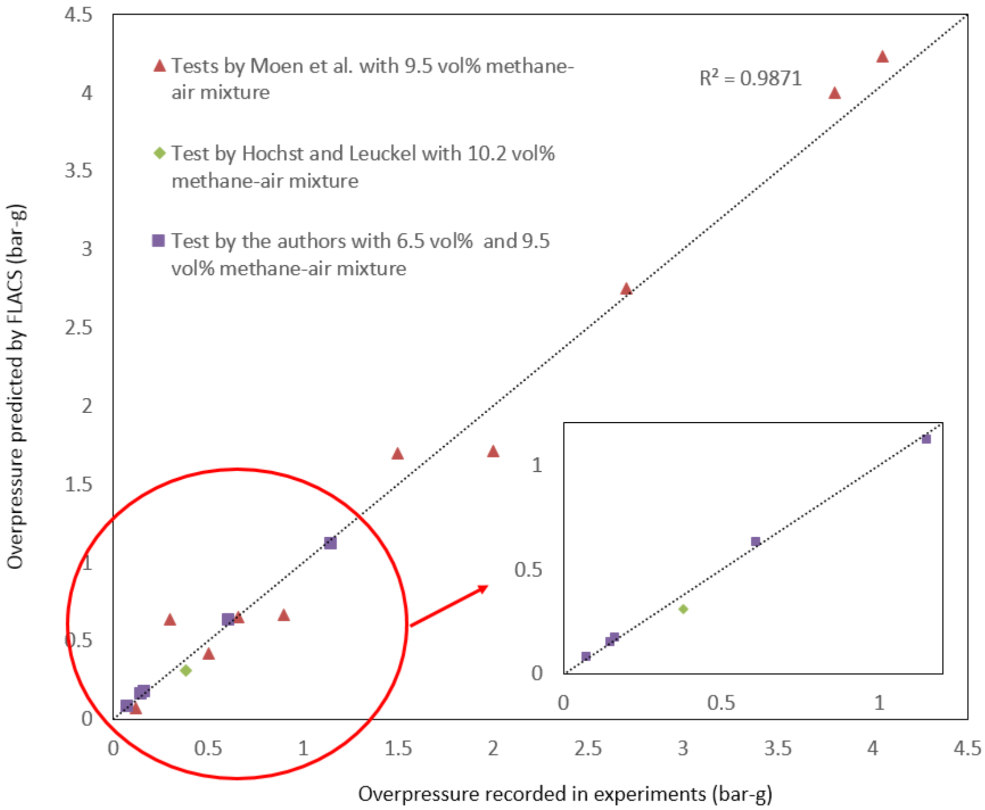

Fig. 18 Comparison of peak overpressures predicted by FLACS and peak overpressures monitored in all experiments carried out by Hochst and Leuckel, Moen et al. and the authors

4. Parametric studies and development of the VMEOC correlations

CFD simulations of both small-scale and large-scale vented methane-air explosions have been validated by comparing with experimental data, the derivation of the new Vented Methane-air Explosion Overpressure Calculation (VMEOC) correlations are then carried out. The primary purpose of developing the VMEOC correlations is to provide engineers an easier and accurate method to predict peak internal overpressure of a vented methane-air explosion with specific initial condition. The phenomenological derivation of the VMEOC is based on the linear least squares method, a subset of more than 350 FLACS simulations are conducted to consider the key parameters including laminar burning velocity, cylindrical enclosure scaling, vent area size and vent pressure resistance, which potentially account for oscillatory combustion, turbulence inducing flame accelerations and Taylor instabilities, etc. It has to be pointed out that the largest cylindrical tank in the simulation has the dimension of 3m diameter and 6m height (i.e. volume of 42.41m^3)

4.1 Parameter of gas-air equivalence ratio

The determination of laminar burning velocity S_u and gas-air concentration in this paper is made according to the inherent gas data model in FLACS (Gexcon, 2015). For a specific gas-air concentration, the laminar burning velocity S_u can be read from Fig. 19. The Equivalence Ratio (*ER*), which is used to measure the gas-air concentration, is defined as below (the stoichiometric methane concentration is 9.5 vol %):

$$\phi_{gas} = \frac{(V_{gas}/V_{air})_{actual}}{(V_{gas}/V_{air})_{stoichiometric}} \tag{13}$$

where V_{gas} is the volume of gas and V_{air} is the total volume of air in the gas-air mixture.

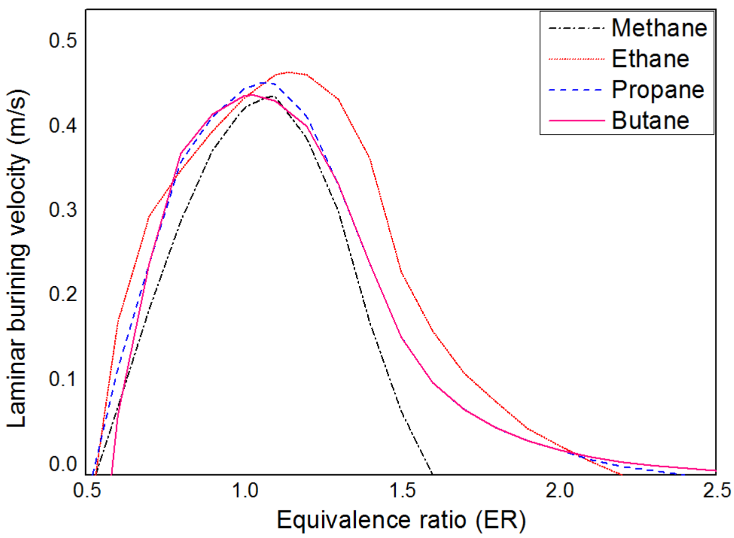

Fig. 19 Laminar burning velocity of individual gas types

48 CFD simulations with 8 varying *ERs* of methane-air mixture, 5 different tank dimensions, 5 different vent sizes and 2 different vent activation pressures are performed. The effect of the *ER* of methane on peak overpressure inside the tank is expressed by using Equation (14), R-squared factor of 94.81% of the correlation between the ER and peak overpressure is seen in Fig. 20.

$$\phi_{gas}^{*} = 3.5\ln\left(-4\left|\ln\left(\phi_{gas} - 0.1\right)\right|^{\left(\frac{1}{\phi_{gas}} + 0.1\right)^{0.7}} - \left|-1 + \phi_{gas}^{\phi_{gas}}\right| + 6\right) - 4.1 + \frac{16.80\left(\frac{P_{act}}{P_{o}}\right)^{0.75}}{V} \qquad (14)$$

where ϕ_{gas} is the equivalence ratio of gas, P_{act} is the vent activation pressure, V is the volume of enclosure, and P_o is the initial enclosure prior to ignition.

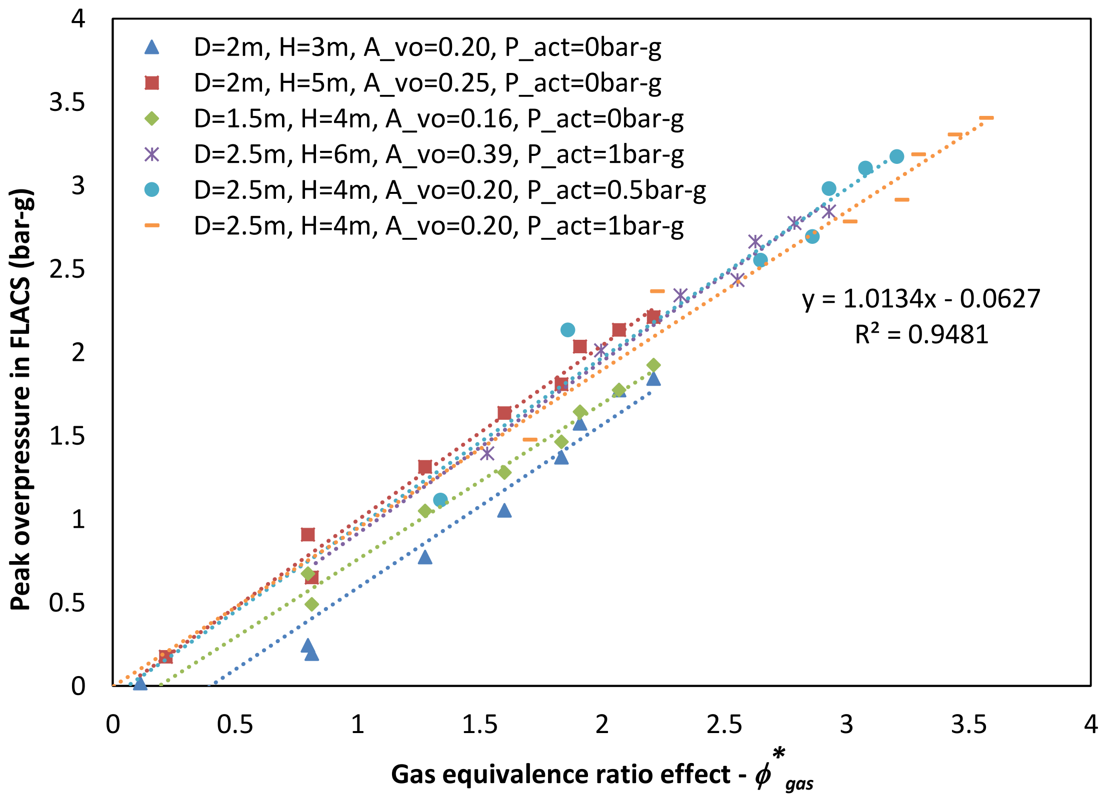

Fig. 20 Gas equivalent ratio effect vs. simulated peak pressure in FLACS

4.2 Parameter of vent activation pressure

The investigation of vent activation pressure's effect on internal peak overpressure of vented gas explosion is then performed by conducting 84 CFD simulations. As seen in Fig. 21, 10 different tank dimensions are included in FLACS simulation, the vent area size is varied from 0.16m^2 to 1.96m^2. The stoichiometric methane concentration of 9.5 vol% is kept constant. Two equations are derived with respect to the ratio of vent area size to the tank dimension, namely:

If $\frac{A_{vo}\mathrm{D}}{A_{rf}H} > 0.04$,

$$P_{act}^{*} = 2.52\ln\left(1 + P_{act}^{1.4}\sqrt{\frac{A_{vo}\mathrm{D}}{A_{rf}H}}\right) + 1.26\,P_o\ln\left(\frac{0.02\,V}{A_{vo}}\right) + 2 \tag{15}$$

If $\frac{A_{vo}\mathrm{D}}{A_{rf}H} \leq 0.04$,

$$P_{act}^{*} = 0.45\,P_{act} + 1.26\,P_o\ln\left(\frac{0.02\,V}{A_{vo}}\right) + 2 \tag{16}$$

where D is the diameter of tank, H is the height of tank, A_{vo} is the vent area size, and A_{rf} is the roof area size.

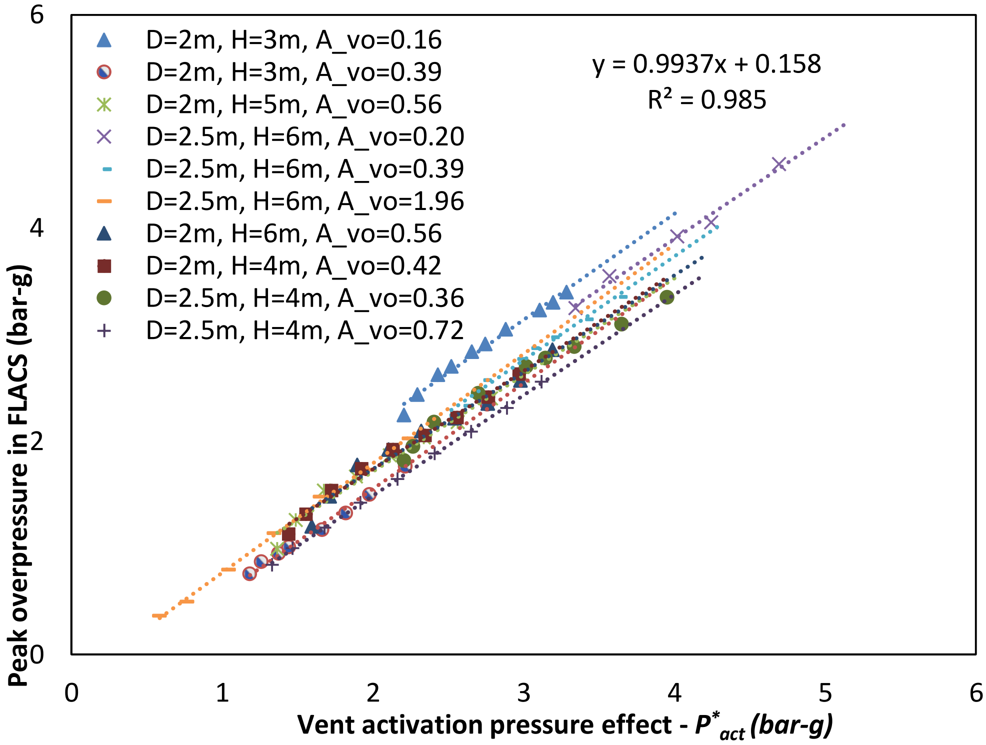

Fig. 21 Vent activation pressure effect vs. simulated peak pressure in FLACS

As shown in Fig. 21, similar slopes are seen for all simulation categories in the investigation of vent activation pressure on peak overpressure. The R-squared factor is 98.5%, indicating a very good fit of the scattered data.

4.3 Parameter of vent area size

According the enclosure length to diameter ratio, the vent area size effect on the peak overpressure prediction of vented methane-air explosion is examined in 2 major categories and 3 groups as given below.

Category 1: $\frac{H}{\mathrm{D}} \geq 3$

$$A_{vo}^{*} = 4.5\left(0.03530 + 0.01765\left(\frac{1}{1.2}\frac{H}{\mathrm{D}} - 1\right)^{2}\right)\mathrm{D}^{1.82} A_{vo}^{\left(-\frac{2\,\mathrm{D}}{H}\right)} - 0.65 \qquad (17)$$

Category 2: $\mathbf{0} < \frac{H}{\mathrm{D}} < 3$

If $0 < \frac{H^2}{D^3} < 1.3$,

$$A_{vo}^{*} = 4 \cdot e^{-\left(\frac{A_{vo}}{A_{rf}} - 0.01\right)\left(\frac{H}{D}\right)^{6.2}} - \frac{4H^2}{D^3} + 4.4 \tag{18}$$

If $1.3 \leq \frac{H^2}{D^3} < 3$,

$$A_{vo}^{*} = \begin{cases} \left(4e^{-\left(\frac{A_{vo}}{A_{rf}}-0.01\right)\frac{H^4}{D^4}}\right)^{\frac{12317}{V^2}} - \dfrac{8.64\times10^{-4}V^{2.15}}{\left(\dfrac{A_{vo}}{A_{rf}}\right)^{0.1}} + 2.8\max\left(\dfrac{H}{D}-2,0\right)+0.4 & \dfrac{A_{vo}}{A_{rf}} > \dfrac{5}{A_{cy}} \\ 4e^{-\left(\frac{A_{vo}}{A_{rf}}-0.01\right)\frac{H^4}{D^4}} + 2.8\max\left(\dfrac{H}{D}-2,0\right)+0.4 & \dfrac{A_{vo}}{A_{rf}} \leq \dfrac{5}{A_{cy}} \end{cases} \tag{19}$$

If $\frac{H^2}{D^3} \geq 3$,

$$A_{vo}^{*} = 4 \cdot e^{-\left(\frac{A_{vo}}{A_{rf}} - 0.01\right)\left(\frac{H}{D}\right)^{2.8}} + 0.4 \tag{20}$$

where A_{cy} is the tank wall surface area.

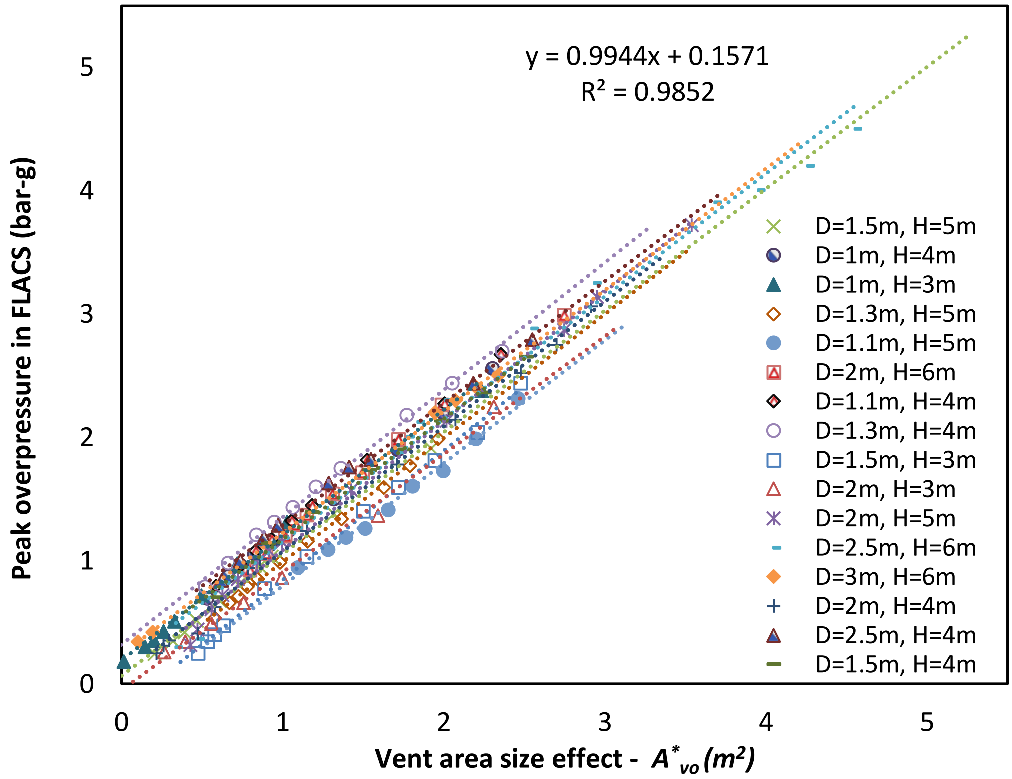

Fig. 22 Vent area size effect vs. simulated peak pressure in FLACS

The relationship between the vent area size effect and internal peak overpressure from the methane-air explosion is shown in Fig. 22, trendlines for all cases have similar slopes and the R-squared factor is about 98.52%. 16 scales with tank volume changing from 2.36m^3 to 42.41m^3 are investigated. For each tank scale, about 12 different vent area cases are modelled. The vent activation pressure and gas concentration are kept constant as 0 bar-g and 9.5 vol%. In total, about 200 CFD simulations are carried out to generate the vent area size correlations.

4.4 New proposed VMEOC correlations

With the influences of the parameters of gas equivalent ratio, vent activation pressure, and vent area size investigated above, the VMEOC correlations are proposed to take the combined effects of the above parameters into consideration. The peak overpressure of a specific vented methane-air explosion can be predicted in two categories, namely, enclosure with small ratio of vent area to tank size and enclosure with large ratio of vent area to tank size:

4.4.1 Enclosure with small vent area ratio ($(A_{vo} / A_{rf}) \cdot V^{1/3} \leq 0.08$)

If $P_{act} = 0$,

$$P_{\max} = 1.613 \ln\left[\left(\phi_{gas}^{*\;\left|1-\ln\left(\phi_{gas}\right)\right|} - 2.1\left|1-\phi_{gas}^{*}\right|\right)\cdot P_{act}^{*}\cdot A_{vo}^{*} + 4\right] - 1.93 \tag{21}$$

If $P_{act} > 0$,

$$P_{\max} = \begin{cases} 1.613\ln\left[\left(\phi_{\text{gas}}^{*\left|1-\ln\phi_{\text{gas}}\right|} - 2.1\left|1-\phi_{\text{gas}}\right|\right)P_{act}^{*}A_{vo}^{*} + 4\right] - 1.93 & 10 \leq \dfrac{\left(\dfrac{H}{D}\right)^{3}}{A_{rf}} \leq 250 \\ 1.613\ln\left[\left(\phi_{\text{gas}}^{*\left|1-\ln\phi_{\text{gas}}\right|} - 2.1\left|1-\phi_{\text{gas}}\right|\right)\left(0.005e^{P_{act}^{*}} + 0.1\dfrac{A_{rf}}{A_{vo}}P_{atm}\right)A_{vo}^{*} + 4\right] - 1.93 & \dfrac{\left(\dfrac{H}{D}\right)^{3}}{A_{rf}} < 10 \\ 1.613\ln\left[\left(\phi_{\text{gas}}^{*\left|1-\ln\phi_{\text{gas}}\right|} - 2.1\left|1-\phi_{\text{gas}}\right|\right)\left(P_{act}^{*} - 9.79\times10^{5}\dfrac{A_{rf}^{2.5}}{V^{7.5}A_{vo}^{7}}P_{atm}\right)^{1.25}A_{vo}^{*} + 4\right] - 1.93 & \dfrac{\left(\dfrac{H}{D}\right)^{3}}{A_{rf}} > 250 \end{cases} \tag{22}$$

4.4.2 Enclosure with large vent area ratio ($(A_{vo} / A_{rf}) \cdot V^{1/3} > 0.08$)

If $P_{act} = 0$,

$$P_{\max} = 1.613 \ln\left[\left(\phi_{gas}^{*\;\left|1-\ln\left(\phi_{gas}\right)\right|} - 2.1\left|1-\phi_{gas}^{*}\right|\right)\cdot\left(3\cdot P_{act}^{*\;0.3} - 1.7\cdot P_{atm}\right)\cdot A_{vo}^{*} + 4\right] - 1.93 \tag{23}$$

If $P_{act} > 0$,

$$P_{\max} = 1.613 \ln\left[\left({\phi^{*}_{gas}}^{\left|1 - \ln\left(\phi_{gas}\right)\right|} - 2.1\left|1 - \phi^{*}_{gas}\right|\right) \cdot {P^{*}_{act}}^{1.6} \cdot A^{*}_{vo} + 4\right] - 1.93 \quad (24)$$

where:

ϕ^{*}_{gas} is the effect of gas equivalence ratio from equation (2),

P^{*}_{act} is the effect of vent activation pressure from equations (3) and (4),

A^{*}_{vo} is the effect of vent area ratio from equations (5)-(8),

P_{atm} is the atmosphere pressure.

4.5 Validation of the VMEOC correlations

The validation of VMEOC is performed by carrying out about 350 CFD simulations. The investigated tank volumes vary from $2.36\mathrm{m}^3$ to $42.41\mathrm{m}^3$, the vent panel area to tank cross section area ratio is in the range of 1.83% - 56.59%, the methane-air concentrations used in FLACS simulations are from 5.7 vol% to 14.25 vol% (namely, ER = 0.6 – 1.5). As shown in Fig. 23, for enclosures with small vent area ratio of $(A_{vo} / A_{rf}) \cdot V^{1/3} \leq 0.08$, the R-squared value yielded by the comparison of VMEOC results and FLACS simulation data is remarkable (97.02%). In terms of the large vent area ratio ($(A_{vo} / A_{rf}) \cdot V^{1/3} > 0.08$) cases, the correlation factor of R-squared value is 88.98%.

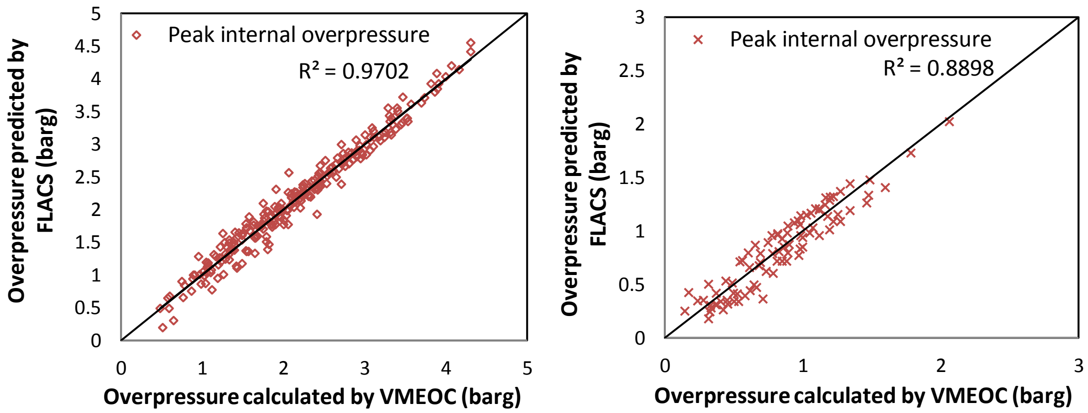

(a) Small vent area ratio enclosures (b) Large vent area ratio enclosures

Fig. 23 R-squared value of VMEOC data vs. FLACS results for vented enclosures subjected to methane-air explosion

5. Comparison of the VMEOC correlations with NFPA-68 2013 edition's new gas venting equations

In order to further validate the accuracy of the VMEOC correlations, these 350 vented methane-air explosions' overpressures predicted by VMEOC above are compared with results calculated by using NFPA-68 2013 edition's equations as well. FLACS simulation is used as the benchmark.

The latest version of NFPA-68 standard uses the laminar burning velocity, scale dependent c value in sub-sonic flow correlations, and scale dependent flame enhancement factor λ in sonic-flow correlations to consider the flame instabilities inside the enclosure and through the vent. Therefore, the calculation accuracy is improved comparing to earlier editions (Rodgers and Zalosh, 2013). However, in order to predict the peak overpressure of vented gas explosion, the calculation procedure by using the new equations becomes complicated, the backward induction has to be used to derive the peak overpressure prediction equations of NFPA-68 2013 edition in this study. Three different equations are specified according to the classification of the flow velocity:

For sub-sonic flow condition (when P_{max} <0.5 barg), the peak overpressure calculation is based on Equation 13 given below:

$$P_{\max} = e^{\frac{1}{S_u - 1.\,\beta_2}\left(2.\left(-8.29\,\theta\,S_u + \theta\,S_u \ln\left(R_f\right) + S_u \ln\left(\frac{S_u\,\beta_1\,As\,\rho^{\frac{0.5\left(\beta_2 + 2\,S_u\right)}{S_u}}\,\mu^{-\frac{\beta_2}{S_u}}\left(\left(0.5\,P_{mo} + 0.5\right)^{\frac{1}{\gamma_b}} - 1\right)}{G_u\,C_d}\right) - 0.105\,S_u - 8.4\,\beta_2 - 2.\ln\left(D_v\right) S_u + \ln\left(D_v\right)\beta_2\right)\right)} \qquad (25)$$

For sonic flow condition, the Taylor expansion is used to express the calculation of peak overpressure in NFPA-68 2013 edition as follows:

If $0.5 \le P_{max} \le 0.9$ barg, the burning velocity $u_v = \sqrt{200000\ P_{\max} / \rho_u}$,

$$P_{\max} = -\left(8.91\, C_d \mathrm{D}_v^2 G_u \left(0.5 P_{act} + 0.5\right)^{10/11} + 26.06 A_s S_u\, \rho\, \mathrm{e}^{-\frac{8.99\,\theta\, Su + 14.51\,\beta_2}{Su}} \left(\frac{\rho\, S_u \mathrm{D}_{he}}{\mu}\right)^{\theta} \beta_1 \left(\frac{\rho\, u_v \mathrm{D}_v}{\mu}\right)^{\frac{\beta_2}{Su}} - 12.36 \mathrm{D}_v^2 G_u\, C_d \right) \Bigg/ \left(4.\ A_s\, S_u\, \rho\, \mathrm{e}^{-\frac{8.99\,\theta\, Su + 14.51\,\beta_2}{Su}} \left(\frac{\rho\, S_u \mathrm{D}_{he}}{\mu}\right)^{\theta} \beta_1 \left(\frac{\rho\, u_v \mathrm{D}_v}{\mu}\right)^{\frac{\beta_2}{Su}} + \pi \mathrm{D}_v^2 G_u C_d \right) \tag{26}$$

If $P_{max} > 0.9$ barg, the burning velocity in the equations equals to unburned gas-air mixture sound speed of 343 m/s, and the peak overpressure expression is:

$$P_{\max} = -\left(8.91\, C_d\, \mathrm{D}_v^2 G_u \left(0.5 P_{act} + 0.5\right)^{10/11} + 26.06 A_s S_u\, \rho\, \mathrm{e}^{-\frac{8.99\,\theta\, Su + 8.67\,\beta_2}{Su}} \left(\frac{\rho S_u\, \mathrm{D}_{he}}{\mu}\right)^{\theta} \beta_1 \left(\frac{\rho\, \mathrm{D}_v}{\mu}\right)^{\frac{\beta_2}{Su}} - 12.36 C_d\, \mathrm{D}_v^2 G_u \right) \Bigg/ \left(4 A_s S_u\, \rho\, \mathrm{e}^{-\frac{8.99\,\theta\, Su + 8.67\,\beta_2}{Su}} \left(\frac{\rho S_u \mathrm{D}_{he}}{\mu}\right)^{\theta} \beta_1 \left(\frac{\rho\, \mathrm{D}_v}{\mu}\right)^{\frac{\beta_2}{Su}} + \pi C_d\, \mathrm{D}_v^2 G_u \right) \tag{27}$$

where:

A_s is the enclosure internal surface area,

S_u is the fundamental laminar burning velocity of gas-air mixture,

ρ is the mass density of unburned gas-air mixture,

G_u is the unburned gas-air mixture sonic flow mass flux = 230.1 kg/m^2/sec,

C_d is the vent flow discharge coefficient = 0.7 or 0.8 for 100% roof vented enclosure,

R_f is the Reynolds number based on the laminar burning velocity,

μ is the unburned gas-air mixture dynamic viscosity,

D_{he} is the enclosure hydraulic equivalent diameter,

D_v is the vent diameter.

Corresponding to the vented methane-air explosion cases in the investigation of VMEOC correlations, the maximum pressure developed in a fully confined enclosure (P_{mo} of 7.4 barg) by ignition of stoichiometric methane-air mixture (9.5 vol% concentration) is adopted (NFPA-68, 2013), the enclosure pressure prior to ignition P_o is equal to the atmosphere pressure of 1 barg. In addition, θ is kept as 0.39, β_1 and β_2 are 1.23 and 0.0487 m/sec, respectively.

The evaluation of required vent area by using NFPA-68 2013 edition's new equations is carried out through iterative calculations, over 350 vented methane-air explosion cases are calculated and the sub-sonic flow and sonic flow explosion overpressure prediction data are summarized in Fig. 24. By comparing with the VMEOC correlations, the overpressure estimation equations of NFPA-68 2013 edition give a poor agreement with the FLACS results. It is seen that NFPA-68 2013 edition tends to over-predict the peak overpressure while the VMEOC provides better estimation comparing with CFD simulation results and the R-squared factor is 97.77% overall. More scattered peak overpressure predictions are seen for NFPA-68 equations. Particularly, the overestimation for sub-sonic flow scenario could be over 2.5 times (e.g. these blue marks on the right hand side of the fitting line as seen in Fig. 24), which is due to the fact that the effect of vent activation pressure on peak overpressure of the vented gas explosion is not considered in NFPA-68 2013 edition's sub-sonic flow equation (i.e. equation (13)).

From the safety design point of view, most facilities virtually require the design internal pressure due to vented explosion as low as possible. Fig. 25 indicates the comparison of the peak overpressures below 1 bar predicted by these equations and FLACS results. It is still obviously seen that NFPA-68 predicted overpressures are more dispersed than VMEOC estimated overpressures in the evaluation.

In addition to the comparison between FLACS simulation results and equation-based data, the experimental results used in the validation of FLACS simulation are also compared with the pressures predicted by the VMEOC correlations and NFPA-68 2013 equations, as seen in Fig. 26. It is shown that the VMEOC correlations tend to over-estimate overpressures, particularly for overpressure under 2 bar. The over-prediction tendency is also seen for overpressures under 1 bar by using NFPA-68 2013 equations. Overall, both of the VMEOC correlations and NFPA-68 2013 equations are conservative in low-pressure estimation for vented gas explosion. However, for high-pressure vented gas explosion, more than 3 times overpressures over-estimation (4 bar predicted by NFPA-68 2013 equations vs. 1.15 bar recorded in experiment) is seen in NFPA-68 2013 equations' scattered data in the comparison. In terms of accuracy, the overpressure prediction of VMEOC correlations for vented cylindrical tanks in the size range of 1.77m^3 to 50m^3 is again proved to be superior to the NFPA-68 2013 equations.

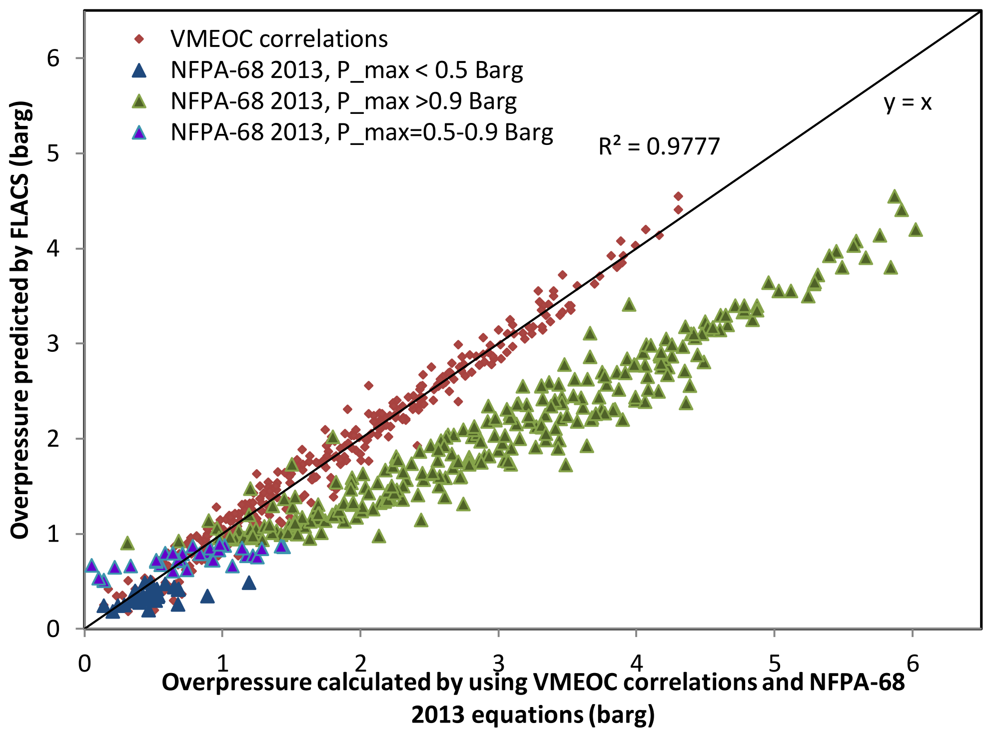

Fig. 24 Comparison of the peak overpressures predicted by VMEOC correlations and NFPA-68 2013 edition's equations vs. FLACS results for vented enclosures subjected to methane-air explosion

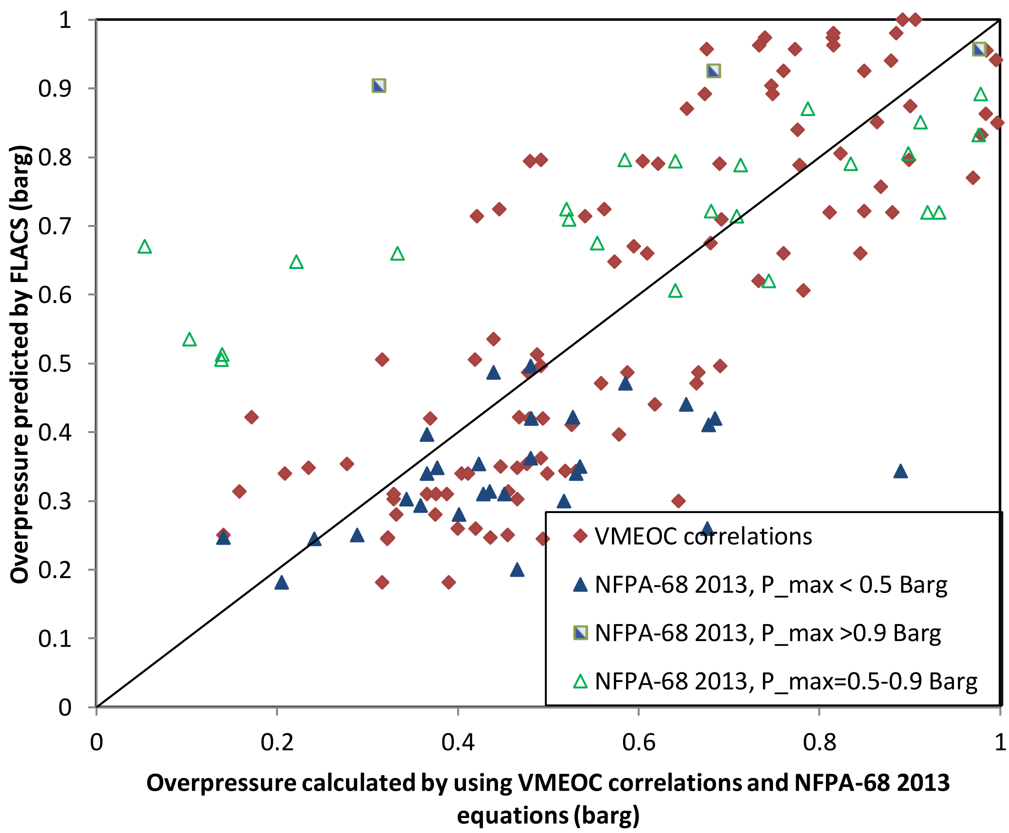

Fig. 25 Comparison of the peak overpressures below 1 bar predicted by VMEOC correlations and NFPA-68 2013 edition's equations vs. FLACS results

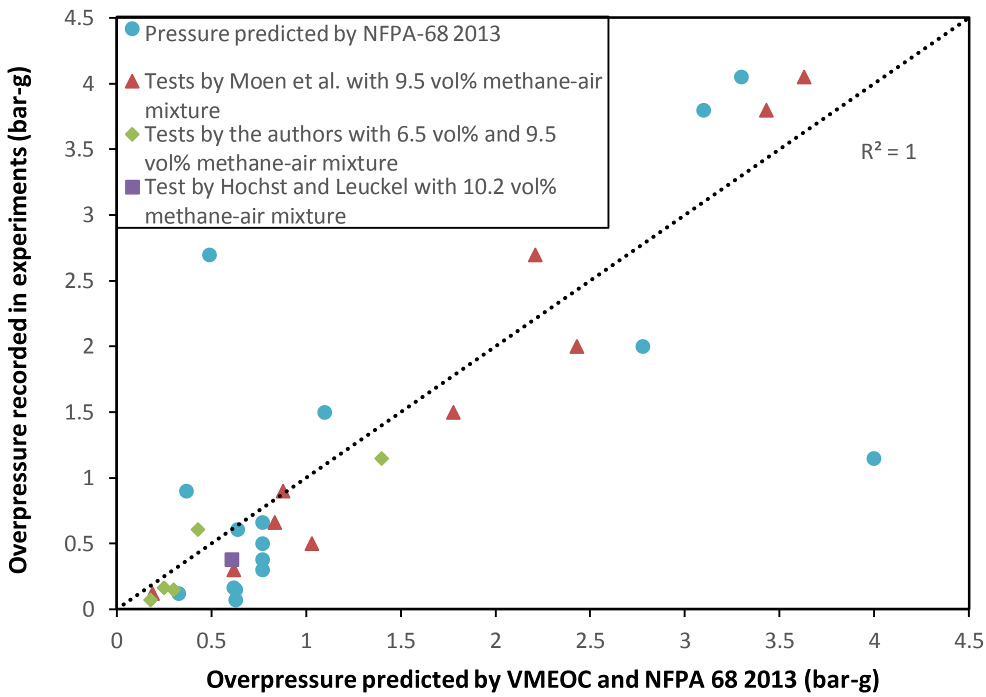

Fig. 26 Comparison of the peak overpressures predicted by VMEOC correlations and NFPA-68 2013 edition's equations vs. experimental results

6. Discussion

In this study, CFD-based VMEOC correlations are developed to calculate peak explosion overpressure. Critical parameters of gas concentration, vent activation pressure, vent area and enclosure geometry are taken into account in the vented gas explosion analysis. The accuracy of VMEOC is demonstrated based on more than 350 CFD simulations by using FLACS.

5 different field blast tests are initially performed by authors. 6.5 vol% and 9.5 vol% methane-air mixtures are used for 3 types of cylindrical tanks with different venting systems. Experimental observation of the influence of vent activation pressure on peak overpressure of vented gas explosion is well recorded. Specifically, the higher vent activation pressure results in greater peak overpressure for enclosures with low

gas concentration, while the effect of vent activation pressure on stoichiometric gas concentration case is negligible. In addition, it is observed that explosions in tanks with large vent areas (e.g. frangible roof case and REMBE panel case) generates instant overpressure drop with shorter time history during the ventilation.

These small-scale experimental results are used to calibrate FLACS simulation in this study. The ignition condition, monitor locations, grid cell size and boundary conditions are thoroughly investigated by conducting sensitivity study in FLACS. CFD models are in one-to-one ratio to realistic vented tank geometries. The pressure-time history data of all FLACS simulations agree well with test results.

Additionally, large-scale test data available in literature are adopted for further validation of FLACS simulation. A cylindrical silo with a volume of $50m^3$ and an ignition on the bottom of the enclosure is numerically modelled. In comparison of the numerical and experimental results, the overpressure-time history of FLACS simulation precisely captures the vent activation pressure, peak pressure and pressure development tendency. Meanwhile, the enclosures with different orifice plate arrangements are modeled in FLACS as well. The confined enclosure volume varying from $8.10m^3$ to $49.09m^3$ and blockage ratio of orifice plate changing from 0% to 84% are examined by using FLACS. Overall, the agreement of peak internal overpressures of the vented methane-air explosion between tests and FLACS simulations is satisfactory.

The VMEOC correlations are then developed using a large number of simulated data with the verified FLACS model for both small-scale and large-scale vented methane-air explosion in cylindrical enclosures. Firstly, the parameter of gas equivalence ratio representing the effects of laminar burning velocity and gas concentration on vented gas explosion is studied. R-squared factor of 94.81% is achieved for the correlation between the *ER* and peak overpressure. Furthermore, two equations regarding the influence of vent activation pressure on vented gas explosion are derived based on 84 CFD modelling cases, and the corresponding R-squared factor is 98.5%. Lastly, over 200 CFD simulations with varying vent area sizes and enclosure volumes are conducted to generate the correlation between the vent area effect and peak overpressure of methane-air mixture explosion.

After taking into account the interactions of all parameters, namely, the gas equivalent ratio, vent activation/opening pressure and vent panel size, the VMEOC correlations are generated. The final correlations to estimate peak internal overpressure are categorized in two groups according to the ratio of vent area to tank dimension. Validation of the VMEOC correlations is performed by summarizing more than 350 CFD modelling cases. R-squared factors of 97.02% and 88.98% are obtained for highly confined enclosure with small vent area ratio and partially confined enclosure with large vent area ratio, respectively.

In addition, the accuracy of NFPA-68 2013 edition's new vented gas explosion equations are studied using the FLACS simulated data as benchmark and compared with VMEOC correlations. The peak overpressure calculation equations in NFPA-68 2013 edition are derived by using backward induction method. The complexity is seen in the iterative calculations of vent area diameter. It is also noteworthy that the vent activation pressure parameter is missing in NFPA-68 2013 edition's sub-sonic flow equation, which results in the significant overestimation of peak overpressure. To sum up, comparing to NFPA-68 2013 edition's equations, the VMEOC correlations provides more accurate peak overpressure calculation results for vented methane-air mixture explosion in cylindrical enclosures.

7. Conclusion

The purpose of this study is to provide engineers a fast and accurate tool to estimate internal overpressure of a vented gas explosion. Therefore, by using the linear least squares method, the VMEOC correlations based on a subset of over 350 CFD simulation cases are phenomenologically developed. The key factors including fundamental burning velocity, enclosure scaling, vent panel size and vent pressure resistance, which potentially account for oscillatory combustion, turbulence inducing flame accelerations and Taylor instabilities are considered in this paper.

Small-scale vented methane-air mixture explosions are experimentally investigated by authors. This series of tests is used along with other large-scale experiments to calibrate FLACS' applicability and calculation accuracy in vented gas explosion. It is observed that FLACS provided satisfactory numerical modelling results that both peak overpressures and overpressure-time history curves are close to experimental data.

Having validated the accuracy of FLACS simulation, the correlations of gas concentration/gas equivalence ratio, vent panel activation pressure and vent size with peak overpressure are then derived by conducting a parametric study. Overall, simulations consist of 16 enclosure scales, 12 vent area to enclosure roof area ratios, 8 gas equivalence ratios and 9 vent activation pressures are considered.

The general correlations of the VMEOC are developed by accounting for the interactions among these key parameters. Two categories of equations are used to calculate the peak internal overpressure for both of highly confined tank with small vent area ratio and partially confined tank with large vent area ratio. In addition the accuracy of the up-to-date NFPA-68 equations of 2013 edition equations are investigated and compared with the newly-developed correlations in this paper. Comparing to NFPA-68 2013 edition, the VMEOC correlations provides an easier way to predict peak overpressure of vented gas explosion. More importantly, higher calculation accuracy of the VMEOC correlations is seen in comparison with the FLACS simulations.

However, this paper focuses on the prediction of vented explosion pressure for cylindrical tanks only, the application of VMEOC correlations is validated in the tank dimension range of $1.77m^3$ to $50m^3$. For cylindrical tank larger than $50m^3$, the newly derived correlations, which relies on CFD modelling by using Reynolds-averaged Navier-Stokes (RANS) equations, can only be used as reference. Additionally, FLACS used in this study is aim to predict the vent activation pressure and the peak pressure due to the external explosion and Taylor instability, while the acoustic waves enhanced peak pressure in not considered. Furthermore, the experimental data obtained by authors are still limited. More tests will be conducted in the future to further validate the accuracy of CFD simulation and the VMEOC correlations. The more advanced Mean Relative Square Error (MRSE) method (SUSANA, 2017) will also be used in the authors’ future validation work.

Acknowledgement

The authors acknowledge partial financial supports from Australian Research Council project (No. LP130100919) and China National 973 project (No. 2015CB058003) for carrying out this research.

References

API-650, 2007. Welded Steel Tanks for Oil Strorage. American Petroleum Institute, 11th Edition.

Arntzen, B.J., 1998. Modelling of turbulence and combustion for simulation of gas explosions in complex geometries, Science and technology division of applied mechanics. The Norwegian University Norway.

Bariha, N., Mishra, I.M., Srivastava, V.C., 2016. Fire and explosion hazard analysis during surface transport of liquefied petroleum gas (LPG): A case study of LPG truck tanker accident in Kannur, Kerala, India. J Loss Prevent Proc 40, 449-460.

Bartknecht, W., 1993. Explosions-Schutz: Grundlagen und Anwendung. Berlin: Springer-Verlag.

Bleyer, A., Taveau, J., Djebaili-Chaumeix, N., Paillard, C.E., Bentaib, A., 2012. Comparison between FLACS explosion simulations and experiments conducted in a PWR Steam Generator casemate scale down with hydrogen gradients. Nucl Eng Des 245, 189-196.

Bradley, D., Mitcheson, A., 1978. The venting of gaseous explosions in spherical vessels. I—Theory. Combustion and Flame 32, 221-236.

Canu, P., Rota, R., Carra, S., Morbidelli, M., 1990. Vented Gas Deflagrations - a Detailed Mathematical-Model Tuned on a Large Set of Experimental-Data. Combustion and Flame 80, 49-64.

Chang, J.I., Lin, C.C., 2006. A study of storage tank accidents. J Loss Prevent Proc 19, 51-59.

Chao, J., Bauwens, C.R., Dorofeev, S.B., 2011. An analysis of peak overpressures in vented gaseous explosions. P Combust Inst 33, 2367-2374.

Cooper, M.G., Fairweather, M., Tite, J.P., 1986. On the Mechanisms of Pressure Generation in Vented Explosions. Combustion and Flame 65, 1-14.

EN-14994, 2007. Gas Explosion Venting Protective Systems. European Standard.

Epstein, M., Swift, I., Fauske, H.K., 1986. Estimation of Peak Pressure for Sonic-Vented Hydrocarbon Explosions in Spherical Vessels. Combustion and Flame 66, 1-8.

Fairweather, M., Vasey, M.W., 1982. A mathematical model for the prediction of overpressures generated in totally confined and vented explosions. Symposium (International) on Combustion, Nineteenth Symposium (International) on Combustion 19, 645-653.

Fakandu, B.M., Andrews, G.E., Phylaktou, H.N., 2015. Vent burst pressure effects on vented gas explosion reduced pressure. J Loss Prevent Proc 36, 431-440.

Ferrara, G., Di Benedetto, A., Salzano, E., Russo, G., 2006. CFD analysis of gas explosions vented through relief pipes. J Hazard Mater 137, 654-665.

Ferrara, G., Willacy, S.K., Phylaktou, H.N., Andrews, G.E., Di Benedetto, A., Salzano, E., Russo, G., 2008. Venting of gas explosion through relief ducts: Interaction between internal and external explosions. J Hazard Mater 155, 358-368.

Gexcon, 2015. FLACS v10.4 User's Manual, Norway.

Guo, J., Wang, C.J., Li, Q., Chen, D.D., 2016. Effect of the vent burst pressure on explosion venting of rich methane-air mixtures in a cylindrical vessel. J Loss Prevent Proc 40, 82-88.

Hansen, O.R., Gavelli, F., Ichard, M., Davis, S.G., 2010. Validation of FLACS against experimental data sets from the model evaluation database for LNG vapor dispersion. J Loss Prevent Proc 23, 857-877.

Hjertager, B.H., 1984. Computer-Simulation of Turbulent Reactive Gas-Dynamics. Model Ident Control 5, 211-236.

Hjertager, B.H., 1993. Computer Modeling of Turbulent Gas-Explosions in Complex 2d and 3d Geometries. J Hazard Mater 34, 173-197.

Hochst, S., Leuckel, W., 1998. On the effect of venting large vessels with mass inert panels. J Loss Prevent Proc 11, 89-97.

Janes, A., Vignes, A., Dufaud, O., Carson, D., 2014. Experimental investigation of the influence of inert solids on ignition sensitivity of organic powders. Process Saf Environ 92, 311-323.

Janovsky, B., Selesovsky, P., Horkel, J., Vejsa, L., 2006. Vented confined explosions in Stramberk experimental mine and AutoReaGas simulation. J Loss Prevent Proc 19, 280-287.

Kurys, A., 2007. Lightning Strikes Wynnewood Oil Refinery, Causing Explosion, Texoma Headlines. KTEN News.

Liang, Y.T., Zeng, W., 2010. Numerical study of the effect of water addition on gas explosion. J Hazard Mater 174, 386-392.

Ma, G.W., Li, J.D., Abdel-Jawad, M., 2014. Accuracy improvement in evaluation of gas explosion overpressures in congestions with safety gaps. J Loss Prevent Proc 32, 358-366.

Mercx, W.P.M., Vanwingerden, C.J.M., Pasman, H.J., 1992. Venting of Gaseous Explosions. Inst Chem E 130, 411-426.

Middha, P., Hansen, O.R., Grune, J., Kotchourko, A., 2010. CFD calculations of gas leak dispersion and subsequent gas explosions: Validation against ignited impinging hydrogen jet experiments. J Hazard Mater 179, 84-94.

Middha, P., Hansen, O.R., Storvik, I.E., 2009. Validation of CFD-model for hydrogen dispersion. J Loss Prevent Proc 22, 1034-1038.

Mitu, M., Prodan, M., Giurcan, V., Razus, D., Oancea, D., 2016. Influence of inert gas addition on propagation indices of methane–air deflagrations. Process Saf Environ 102, 513-522.

Moen, I.O., Lee, J.H.S., Hjertager, B.H., Fuhre, K., Eckhoff, R.K., 1982. Pressure Development Due to Turbulent Flame Propagation in Large-Scale Methane-Air Explosions. Combustion and Flame 47, 31-52.

Molkov, V., Dobashi, R., Suzuki, M., Hirano, T., 1999. Modeling of vented hydrogen-air deflagrations and correlations for vent sizing. J Loss Prevent Proc 12, 147-156.

Molkov, V.V., Grigorash, A.V., Eber, R.M., Tamanini, F., Dobashi, R., 2004. Vented gaseous deflagrations with inertial vent covers: State-of-the-art and progress. Process Saf Prog 23, 29-36.

NFPA-68, 1978. Explosion venting. National Fire Protection Association, Quincy, MA.

NFPA-68, 1988. Guide for venting of deflagrations. National Fire Protection Association, Quincy, MA.

NFPA-68, 1998. Guide for venting of deflagrations. National Fire Protection Association, Quincy, MA.

NFPA-68, 2007. Standard on Explosion Protection by Deflagration Venting, 2013 Edition. National Fire Protection Association, Quincy, MA.

NFPA-68, 2013. Standard on Explosion Protection by Deflagration Venting, 2013 Edition. National Fire Protection Association, Quincy, MA.

Patankar, S.V., 1980. Numerical heat transfer and fluid flow. Hemisphere publishing corporation, London.

Pedersen, H., Tomlin, G., Middha, P., Phylaktou, H., Andrews, G., 2012. Comparison of FLACS simulations against large-scale vented gas explosion experiments in a twin compartment enclosure, Ninth International Symposium on Hazard, Prevention and Mitigation of Industrial Explosions.

Pedersen, H.H., Middha, P., 2012. Modelling of Vented Gas Explosions in the CFD tool FLACS. Chem Engineer Trans 26, 357-362.

REMBE, 2015. Explosion Safety Product Information.

Rodgers, S.A., Zalosh, R., 2013. NFPA 68 - New Gas Venting Equations. AIChE 9th Global congress on process safety.

Rota, R., Canu, P., Carra, S., Morbidelli, M., 1991. Vented Gas Deflagration Modeling - a Simplified Approach. Combustion and Flame 85, 319-330.

Runes, E., 1972. Explosion venting. Loss Prevention, AIChE 6, 68-73.

Sanchez, R., 2014. New York explosion exposes nation's aging and dangerous gas mains. CNN.

Shirvill, L.C., 2004. Efficacy of water spray protection against propane and butane jet fires impinging on LPG storage tanks. J Loss Prevent Proc 17, 111-118.

Siwek, R., 1996. Explosion venting technology. J Loss Prevent Proc 9, 81-90.

SUSANA, 2017. The CFD Model Evaluation Protocol - Fuel Cells and Hydrogen, http://support-cfd.eu.

Swift, I., 1989. Nfpa-68 Guide for Venting of Deflagrations - Whats New and How It Affects You. J Loss Prevent Proc 2, 5-15.

Swift, I., Epstein, M., 1987. Performance of low pressure explosion vents. Plant/Operation Progress 6, 98-105.

Tamanini, F., Chaffee, J.L., 1992. Turbulent vented gas explosions with and without acoustically-induced instabilities, Symposium (International) on Combustion. Elsevier, pp. 1845-1851.

Tomlin, G., Johnson, D.M., Cronin, P., Phylaktou, H.N., Andrews, G.E., 2015. The effect of vent size and congestion in large-scale vented natural gas/air explosions. J Loss Prevent Proc 35, 169-181.

Ugarte, O.J., Akkerman, V., Rangwala, A.S., 2016. A computational platform for gas explosion venting. Process Saf Environ 99, 167-174.

Wang, Z., Pan, Y., Yan, J., 2006. Simulating safety design of bursting disc for venting of gas explosion. Chemical Engineering of Oil & Gas 6, 23.